

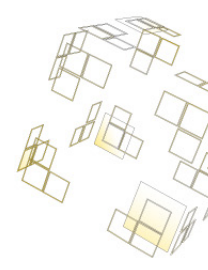


# DOA Estimation of UHF RFID Tags in Multipath Environments

Yoppy

(S1347438)

Master's Thesis



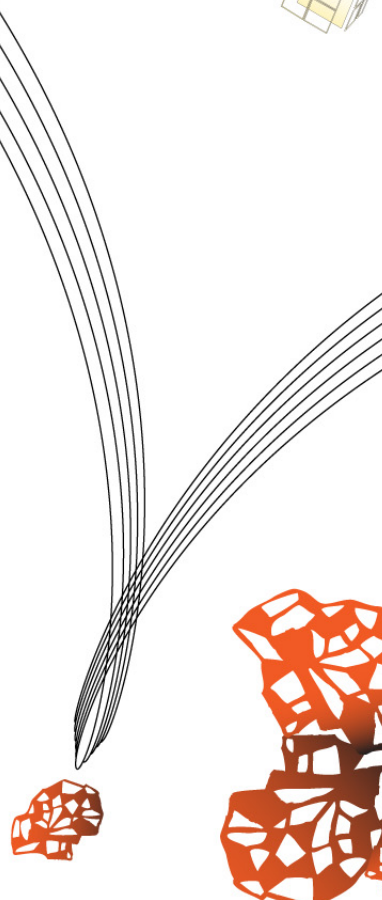
## Graduation Committee:

dr. ir. A.B.J. Kokkeler

J. Huiting, MSc

ir. E. Molenkamp

ir. J. Scholten



Chair of Computer Architecture and Embedded Systems (CAES)

Faculty of Electrical Engineering, Mathematics, and Computer Science

University of Twente

**UNIVERSITEIT TWENTE.**



# Contents

<b>Acknowledgements</b>	<b>1</b>
<b>Abstract</b>	<b>3</b>
<b>1 Introduction</b>	<b>5</b>
1.1 RFID in retail environments . . . . .	5
1.2 DOA estimation of UHF RFID tags . . . . .	6
1.3 Research question . . . . .	7
1.4 Scope . . . . .	7
<b>2 Theoretical Backgrounds</b>	<b>9</b>
2.1 Overview of RFID communication protocol . . . . .	9
2.2 Phased-Array . . . . .	13
2.3 DOA Estimation Algorithms . . . . .	16
2.3.1 Beamforming techniques . . . . .	16
2.3.2 MUSIC algorithm . . . . .	18
2.4 Multipath Environments . . . . .	19
2.5 Number of Signals Detection . . . . .	25
2.6 Underestimating vs Overestimating Number of Signals . . . . .	28
<b>3 Implementation</b>	<b>31</b>
3.1 Applicability of phased-array to Gen 2 UHF RFID . . . . .	31
3.2 Hardware implementation . . . . .	31
<b>4 Measurements and Analysis</b>	<b>37</b>
4.1 Number of signals estimation . . . . .	38
4.2 Effect of calibration . . . . .	39
4.3 Measurements in reflection-minimum environments . . . . .	40
4.4 Measurements in reflective environments . . . . .	43
<b>5 Conclusions</b>	<b>47</b>
<b>6 Recommendations</b>	<b>49</b>
<b>7 Appendix</b>	<b>51</b>
<b>Bibliography</b>	<b>61</b>



# Acknowledgements

I would like to express my gratitude to Andre Kokkeler for his excellent guidance and critical feedback on my report; Jordy Huting for his support, starting from the visit during my internship at Nedap, relocating the setup from Nedap, assisting in the measurements, guidance during the thesis work, to substantial suggestions on my report; Bert Molenkamp for being a great academic supervisor who cares about every detail; Rembrand Lakwijk for his awesome piece of work and nice documentation; CAES group for the good time, especially the outing day to the Grolsch factory in Boekelo; Prithivi Ram Duraisingam, Xiaopeng Jin, Frank Thomas, Vignesh Raja Karrupiah Ramachandran (hopefully *no typo*), and Gebremedhin Abreha for the time spent together to meet deadlines!

I would not have passed this two years of highly demanding Dutch education without spiritual and emotional supports. So I want to thank the International Christian Fellowship Enschede (ICFE) for providing the food for my soul. My gratitude also goes to the Indonesian student association (PPIE) and all Indonesian students who frequently organize gathering and cooking Indonesian food. So, I almost never feel homesick.

I am also grateful to Femi Ojambati for providing me a shelter for the last two months and also being a good friend. I am happy that I have the opportunity to live in a residential area. Working in the garden, cleaning the house, and eating while looking at the window view are nice things to do. Of course, the best part is strolling in the afternoon (it's summer!)

All these dream-comes-true experiences would not be possible without the support from the scholarship sponsor, Kemenkominfo RI, particularly TPSDM. Thanks for the excellent organization and support from the beginning till the end. Of course, my sincere appreciation is also addressed to my colleagues in P2SMTP-LIPI for their help and support.

If I have enough space, I would mention all the great people one by one. But I do not.

So I want to save this last space to thank my family for their love.

Enschede, 27 August 2014



# Abstract

Inventory management is a crucial aspect in retail businesses. The idea is to keep tracking the stock quantity as well as the location of each item whether it is in the front shop or in the store room. By maintaining the stock availability, opportunity loss can be prevented.

Although inventory management is still dominated by barcode systems, RFID based systems are now becoming more widely used. This is due to the advantages offered by RFID systems such as faster reading time, higher data capacity, and no direct visibility requirement.

To achieve high efficiency, it is desirable to have a system that can automatically read the identification number as well as the direction of movement of each item while it is being relocated, for example from the store room to the front shop, and *vice versa*. Such a system is usually implemented as a combination of an RFID system and an infrared transmitter and receiver pair installed on a gate. This system, however, only allows movement from one direction at a time. In order to be able to detect both directions at the same time, a new method using a phased array was proposed.

A six-element linear phased array has been implemented. Measurements in reflection-minimum environments showed that the direction of arrival (DOA) estimations were good and consistent. However measurements in reflective environments, comparable to retail shops, showed deteriorated results. Such worsening results were most likely caused by the presence of multipath signals.

While showing a promising simulation result in solving multipath signals, the forward/backward spatial smoothing (FBSS) algorithm was unfortunately not able to improve the real measurement in the reflective environments. This is probably because the number of antennas is insufficient and the multipath signals are too closely spaced.



# 1 Introduction

## 1.1 RFID in retail environments

In the fast growing business nowadays, production, distribution, and retailing are becoming much more challenging. Driven by high speed and large quantity demands, those business activities require some kind of automated systems. It is not only about machinery and more streamlined production processes, but also about reliable identification systems. Automatic identification coupled with database systems allows more efficient product inventory and monitoring.

Until now automatic identification systems are still dominated by barcode systems. It has enjoyed high popularity since its inception several decades ago. This is due to its simplicity and low cost. For example it has been used extensively for point-of-sale and inventory management in retail shops. In manufacturing and distribution sites, automatic identification is also a crucial part to achieve an efficient supply chain management. Nevertheless the barcode system has two major limitations, i.e. very small data capacity and restricted line of sight [Fin10]. To make the case clear, the following example is taken from a clothing shop in Japan [epc14], and is undoubtedly also common to retail shops in general. When a box containing a large quantity of clothes arrives at the shop, the shopkeeper is to inventorize all the items inside the box. Because of small data capacity, the barcode attached to the box cannot be used to store the item information on individual basis. Therefore, the box needs to be unpacked, and the items are scanned. Moreover, a barcode reader is an optical system that requires a close and direct visibility to the barcode label. Therefore, inventory activities can be time consuming and labor intensive.

It is known that radio frequency systems have an edge over optical systems. Unlike optical systems, radio frequency ones do not require close and precise line of sight. This is an attractive feature where radio frequency identification (RFID) comes into play. Since an RFID reader can read tags (or labels) in a distant location, presenting the tags individually to the reader is not necessary. This can substantially reduce human intervention. Moreover, a silicon chip is also embedded in the tag, which can be used to store much more digital information. With these features, RFID systems are more expensive than barcode systems whose labels are merely a matter of printing. However, considering the time and labor efficiency gained, overall RFID can be more advantageous than barcode. Also, the prices of RFID tags show a declining trend as many more companies implement RFID systems.

## 1.2 DOA estimation of UHF RFID tags

In retail environments, typically there are a store room, front shop, and checkout counters. A crucial aspect in retail businesses is product inventory. It is important to always ensure the product availability, whether it is by relocation from the store room to the shop if the product is still in stock, or purchasing from wholesalers when it is almost out of stock. Moreover, prediction about certain products demand in special seasons can be made based on previous sales. So, retailers can stock the right quantity. By monitoring the product availability constantly and take necessary actions, opportunity loss can be minimized and more profits can be gained.

Although such product inventory systems nowadays are still dominated by barcode systems, RFID has been increasingly employed because of the superiority in terms of unrestricted line of sight, bigger data storage capacity, and faster scanning time. However, RFID has its drawbacks. Some systems deploy multiple RFID readers to cover the whole room and the products will be scanned automatically. This system obviously comes at high cost. Another system may use a single reader with much stronger power, but it may not comply with the telecommunication regulations regarding power limits. Another solution is to use a handheld RFID reader and scan the products manually on regular basis. But manual scanning can be time consuming and therefore costly [vL13].

Instead of covering the whole area in the rooms, another strategy is to keep track of the product movement between the rooms, whether it is between the store room and front shop, or between the front shop and checkout counters. This simpler solution is implemented by coupling RFID with a photo-gated system, where the gate is equipped with two sets of photo sensors to detect direction of movement whether it is going out or coming in. Unfortunately this system does not work when two persons or objects are passing through the photo-gate from opposite directions. In addition, a false read may occur when a tag is outside the read range but is somehow being read, e.g. because of metal reflection, and at the same time the photo-gate is passed through by an object or person [vL13].

An alternative solution employing phased-array Direction of Arrival (DOA) estimation was proposed in [vL13]. The idea is to install a phased-array on a gate ceiling and keep tracking the tags DOA in the vicinity to determine their movement direction, be it coming in or going out. The applicability of phased-array DOA estimation in UHF RFID 865-868 MHz has been studied [vL13]. A four-element uniform linear array (ULA) was implemented, and the details can be found in chapter 3.

To test the system's performance, several DOA algorithms were put on trials, i.e. far-field MUSIC, near-field MUSIC, root-MUSIC, ESPRIT-LS, and ESPRIT-TLS. The measurements were carried out in a large empty room. The tag was suspended at three different heights right above the reader, i.e 50 cm, 75 cm and 100 cm. At each height, the tag was moved horizontally to the left and the right with intervals of 5 cm within an end-to-end range of 150 cm. Overall, the MUSIC algorithm gave

the best accuracy with root mean square error (RMSE) less than  $14.3^\circ$ ,  $2.8^\circ$ , and  $7^\circ$  for 50 cm, 75 cm and 100 cm tests, respectively. However, a closer look at the DOA estimations at individual positions reveals that unacceptably large outliers occur at some points.

Furthermore, experiments on greater tag-reader distances within the read range were also carried out, yet undocumented in [vL13]. Ideally, the greater the tag-reader distance, the better the far-field assumption is complied. But it was surprising that when the tag-reader distance was further increased, the performance tended to become worse. This was indicated by the presence of more outliers.

## 1.3 Research question

One possible explanation for the deterioration mentioned above is because the presence of multipath signals. Multipath is known to cause subspace based DOA algorithms like MUSIC to fail. Another potential explanation is due to the array not being calibrated. An uncalibrated array could introduce unwanted phase shifts, and so the data do not truly represent the signal's phase information anymore.

Contemplating the above problems, this research is aimed to address the question:

How can we improve the current four-element phased array to achieve more consistent and accurate DOA estimations of RFID tags in multipath environments?

## 1.4 Scope

In a realistic retail environment, it is by nature that numerous tags are in the read range of the reader. Consequently, after a DOA is estimated, it needs to be associated with the corresponding tag identification number. By doing so, the movement of every tag can be tracked. Moreover, it is quite typical that line of sight (LOS) is not available, for example when clothes are put in stack, or in a box. In addition, it is not uncommon in retail shops to have multiple readers operating nearby.

However the scope of this research is constrained to the case of a single tag, available LOS, and a single operating reader.



# 2 Theoretical Backgrounds

## 2.1 Overview of RFID communication protocol

The book *The RF in RFID* written by Daniel Dobkin provides a comprehensive guide on the radio aspect of the RFID technology. This section is mainly summarized from the book. Figure 2.1–Figure 2.6 are taken from the book as well.

Although RFID systems can operate on any frequency, widely used RFID standards only occupy small portion of the spectrum. In the low frequency (LF) region, RFID operates at 125/134 kHz. Whereas in the high frequency (HF) band, most commonly found RFID protocol works at 13.56 MHz. In the ultra high frequency (UHF) band, there are two most common frequency sub-bands, namely 860-960 MHz and 2.4-2.45 GHz [Dob08].

In the LF and HF band, where the size of the antenna is much smaller than the wavelength, RFID operates in inductive coupling mode. In principle, inductive coupling is similar to that of a transformer. The reader's signal induces a voltage to the tag, and in response the tag *disturbs* (or modulates) the reader's electromagnetic field. The reader then senses this modulation and extracts information from it. In inductive coupling mode, the power of the reader's signal decreases extremely fast as the distance between tag and reader increases. So it suits best in short range applications. On the other hand, UHF systems operate in radiative coupling mode and have a wider coverage area.

LF RFID has a short read range, that is less than 1 m, and is only capable of low data rates around 1 kbps. LF RFID is commonly used in livestock management. The tag can be attached to the animal's body or inserted under the skin. Using higher frequencies, HF RFID can transfer higher data rates up to tens of kbps. The application of HF RFID can be found in smart cards for transportation ticketing, personal identity cards, and passports. UHF offers the highest data rates up to several hundreds kbps and a read range of 1-10 m. A battery-powered tag system even covers a radius of several hundreds meters. UHF RFID is widely used in supply chain management, asset management, and inventory in retail shops [Dob08].

### EPCglobal Class 1 Generation 2

Many RFID communication protocols have been developed over the years. The latest one is EPCglobal Class 1 Generation 2, which is also approved as ISO 18000-

6C. EPCglobal Class 1 Generation 2 or *Gen 2*, for short, regulates UHF RFID with frequency operations from 860 to 960 MHz. Under European Telecommunication Standards Institute (ETSI) regulations, UHF RFID devices are allowed to operate from 865 to 868 MHz. This band is divided into 15 channels of 200 kHz each.

### Communication from reader to tags

The **reader to tag** signal modulation of Gen 2 can be a simple amplitude modulation (ASK), phase reversal ASK, or phase (PSK) modulation. Figure 2.1 shows a reader to tag communication with ASK modulation. With ASK modulation, the tag can relatively easily demodulate the signal using an envelop detector which consists of a diode and capacitor. Data from the reader is encoded using pulse interval encoding (PIE). A symbol '0' is made up of a low and high state with equal duration. The duration of a symbol '0' is termed *Tari* (see Figure 2.2), whereas pulse width PW is half of *Tari*. A symbol '1' also consists of an on and off state, where the off state is as long as PW but the on state is longer, ranging from 1-1.5 *Tari*. So, sending the symbol '1' takes longer than the symbol '0'. *Tari* is variable to several values, i.e 6.25, 12.5, or 25  $\mu\text{s}$ .

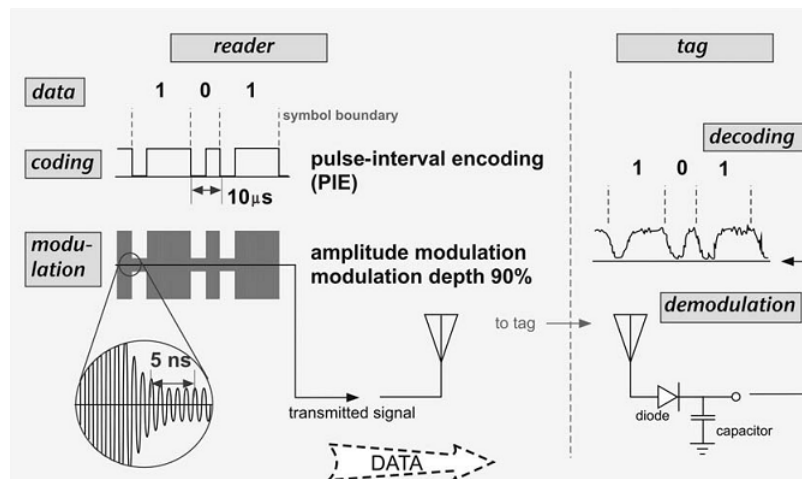


**Figure 2.1:** Reader to tag downlink communication

Gen 2 is an RFID standard for passive and semi-passive tags which harness the reader's signal to transmit information back. As shown in Figure 2.3, a reader keeps transmitting a continuous wave (CW) while listening the response from a tag. The tag modulates and backscatters the CW signal.

### Communication from tags to reader

Instead of using PIE, **tag to reader** communication employs different encoding schemes, whether it is FM0 or Miller modulated subcarrier (MMS). In FM0 encoding, a symbol '0' and '1' have equal duration, called *Tpri*. A symbol '0' has a state

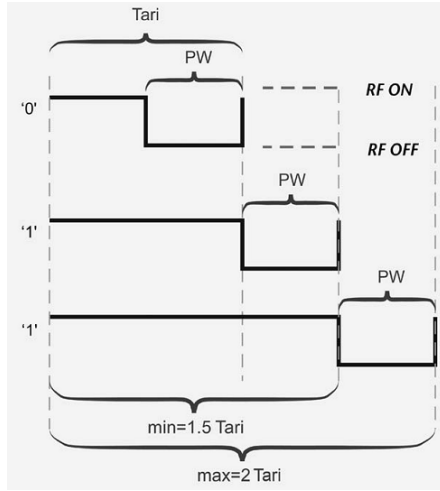


Figure 2.2: Reader-to-tag symbol

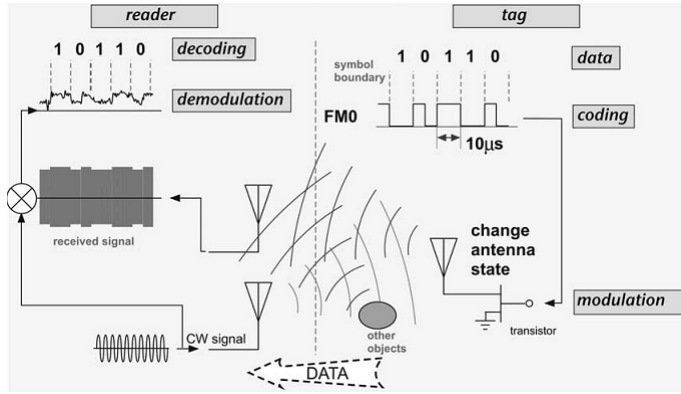


Figure 2.3: Tag to reader uplink communication

inversion in the middle of the symbol, whereas a symbol '1' does not. Intersymbol transitions, whether it is between the same or opposite symbols, always flip state (see Figure 2.4). The transmission terminates with an extra symbol '1' and then stays in the low state. The symbol rate is equal to the inverse of  $T_{pri}$ , which is known as *backscatter link frequency* (BLF).

MMS encoding is more complex than FM0, but it produces a narrower sideband. Baseband formation in MMS encoding is similar to that of FM0, except that a symbol '1' has a state inversion in the middle of the symbol, while symbol '0' does not (see Figure 2.5). MMS then applies another stage of encoding to the baseband signals. A square wave subcarrier with period  $T_{pri}$  is used to modulate the baseband. The subcarrier is phase inverted whenever the baseband is at low state, and stays unaltered while the baseband at high state. In short, MMS encoding is a digital multiplication between the baseband signal and the subcarrier. Note that the duration of one symbol has become longer, i.e.  $M$  multiplicity of  $T_{pri}$ .  $M$  can be 2, 4, or 8.

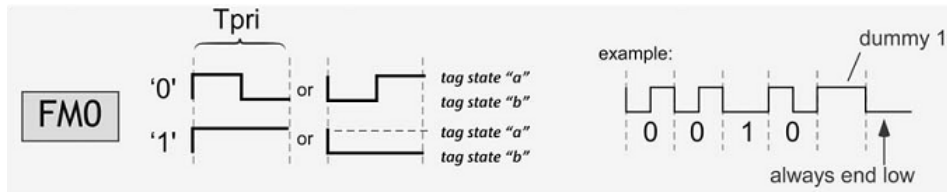


Figure 2.4: Tag-to-reader FM0 encoding

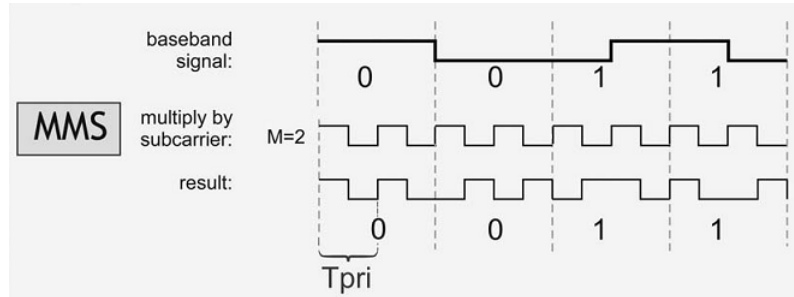


Figure 2.5: Tag-to-reader MMS encoding

At a glance, MMS encoding may look trivial. But observing the resulting spectrum, an interesting feature is revealed. Figure 2.6 depicts FM0 and MMS spectra of 160 random symbols at BLF=125 kHz. It is clear that MMS encoding results in a narrower band centered at the BLF. Therefore, an RFID receiver can obtain a higher tag SNR by filtering the tag signal at a narrower band. By doing so, multiple readers are allowed to operate in the vicinity, which is not uncommon in many application areas, including retail.

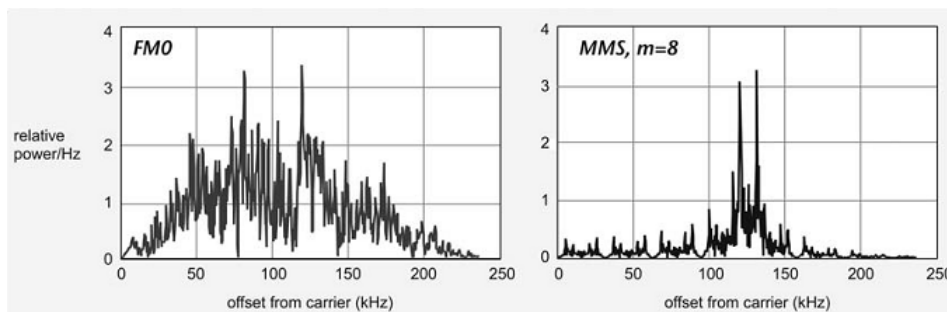


Figure 2.6: FM0 and MMS spectrum comparison

## IQ demodulation

Backscattering signals received by an RFID reader are demodulated to get the baseband signal back. This baseband signal is usually represented in *inphase-quadrature* (IQ) format. As shown in Figure 2.7 the backscattering signals contain two frequency components, namely the continuous wave  $f_{CW}$  and the baseband  $f_{data}$ .

These input signals are downmixed against the local oscillator which has the same frequency as  $f_{CW}$ . The local oscillator is splitted into two signals, i.e. the unaltered and the  $90^\circ$  phase shifted signals. The former will downmix the input signal to produce the *inphase* (I) component, whereas the latter is used to generate the *quadrature* (Q) component. Since the continuous wave  $f_{CW}$  and the local oscillator are at the same frequency, the output of the mixers will consist of a DC component, the baseband signal, and the upper image frequencies. This DC part shifts the IQ data clusters off-center, as shown in the IQ constellation. In order to get the proper IQ clusters at the center and to remove unwanted high frequency components, the mixers' output is then bandpass filtered.

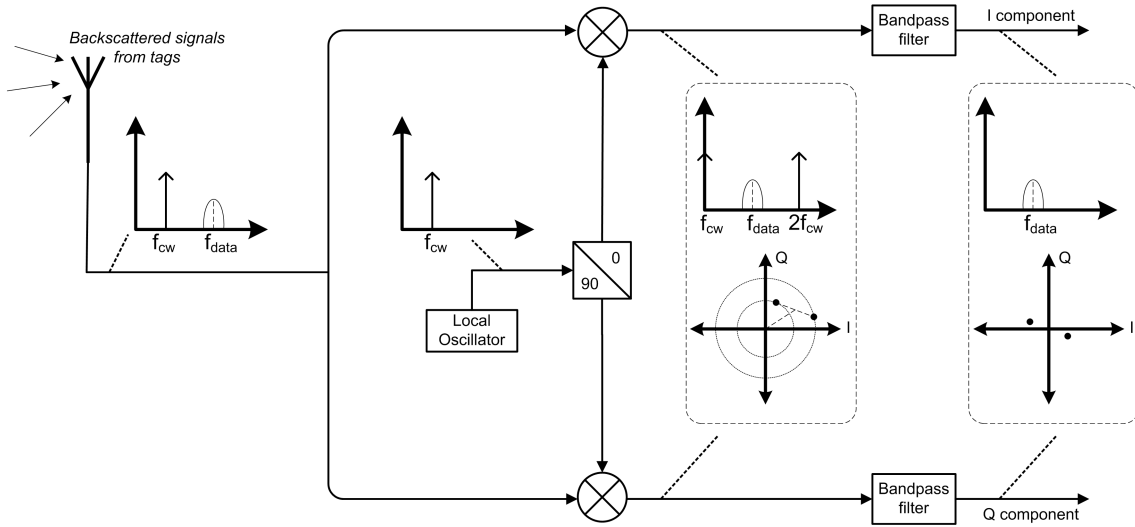


Figure 2.7: IQ demodulation in the RFID receiver [BBR13, Ins13]

## 2.2 Phased-Array

Antenna arrays have long been used for estimating direction of arrival (DOA) of signals, be it acoustic or electromagnetic. Many algorithms have been proposed to *extract* the DOA of signals received at the antenna array. Basically these algorithms assume the following properties [ZCY10]:

1. Isotropic and linear transmission medium

This property guarantees that irrespective of the DOAs, the signals are governed by uniform propagation properties. It ensures that signals do not undergo refractions, which can change the signals' speed, while they are travelling across the antenna array.

2. Far field assumption

The second property states that the signals are radiated far enough from the antenna array such that the signals exhibit a planar wavefront when they

impinge the antenna elements. According to [Ban], the far-field assumption is satisfied when  $r$ , the distance between the signal source and the antenna:

$$r > \frac{2D^2}{\lambda} \quad (2.1)$$

with the constraint  $r > 5D$  and  $r > 1.6\lambda$ , where  $D$  is the length of the array, and  $\lambda$  is the signal wavelength.

Figure 2.8 shows an  $M$ -element uniform linear array. Adjacent elements are spaced at a distance  $d$ , which is usually set to half of the carrier signal's wavelength. The signal is coming from direction  $\theta$  with regard to the line perpendicular to the array structure. Because of the planar wavefront approximation, the signal travels from one element to another as far as distance  $x$ , and by applying trigonometric rules,  $x = d \sin\theta$ . Therefore the time needed to travel along distance  $x$  is

$$\Delta t = \frac{d \sin\theta}{c} \quad (2.2)$$

where  $c$  is the speed of light.

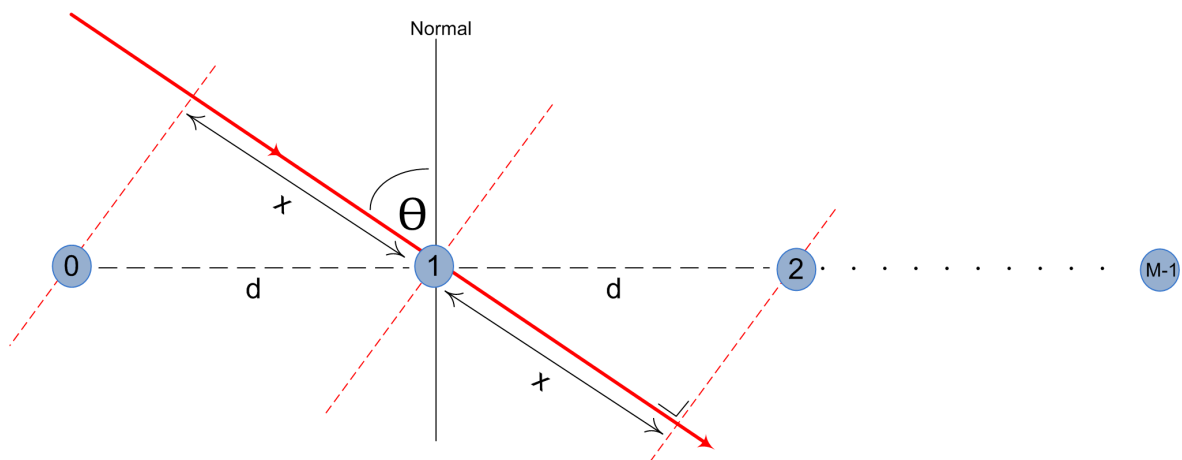


**Figure 2.8:** Antenna array model

### 3. Narrowband assumption

From a time domain point of view, narrowband means that the inverse of the baseband signal bandwidth is much greater than the time needed by the signal to propagate over the length of the array structure. In other words, while travelling across the array, the signal is not varying too much so every antenna element receives identical but a phase-shifted version of the data.

Let  $x_i(t)$  be a modulated narrowband signal received by the  $i$ th antenna element at time  $t$ :

$$\begin{aligned} x_i(t) &= u(t - \Delta t_i) e^{j2\pi f_c(t - \Delta t_i)} \\ &= u(t - \Delta t_i) e^{-j2\pi f_c \Delta t_i} e^{j2\pi f_c t} \quad i = 0, 1, 2, \dots, M - 1 \end{aligned} \quad (2.3)$$

where  $u(t)$  represents the baseband signal,  $f_c$  denotes the carrier frequency, and  $\Delta t_i$  is the time needed to reach element  $i$  relative to the first element of the array structure. By downmixing Equation 2.3 as well as applying the narrowband assumption, where the baseband is relatively constant within a duration of  $\Delta t_i$ , the received baseband can be expressed as:

$$x_i(t) = u(t) e^{-j2\pi f_c \Delta t_i} \quad (2.4)$$

By substituting Equation 2.2 in Equation 2.4,  $x_i(t)$  becomes:

$$\begin{aligned} x_i(t) &= u(t) e^{-j2\pi f_c \frac{id \sin \theta}{c}} \\ &= u(t) e^{-j2\pi \frac{id \sin \theta}{\lambda}} \end{aligned} \quad (2.5)$$

For a half wavelength spaced linear array where  $d = \lambda/2$ , Equation 2.5 can be simplified as:

$$x_i(t) = u(t) e^{-j\pi i \sin \theta} \quad i = 0, 1, 2, \dots, M - 1 \quad (2.6)$$

To model a realistic environment, a zero-mean uncorrelated noise component  $n_i(t)$  is added to Equation 2.6. So the signal model of an  $M$ -element uniform linear array impinged by a single signal is formulated as:

$$x_i(t) = u(t) e^{-j\pi i \sin \theta} + n_i(t) \quad i = 0, 1, 2, \dots, M - 1 \quad (2.7)$$

Equation 2.7 can be extended to the case of  $D$  signals,  $u_1(t), u_2(t), \dots, u_D(t)$  originating from direction  $\theta_1, \theta_2, \dots, \theta_D$  and expressed as follows:

$$\begin{aligned} x_i(t) &= u_1(t) e^{-j\pi i \sin \theta_1} + u_2(t) e^{-j\pi i \sin \theta_2} + \dots + u_D(t) e^{-j\pi i \sin \theta_D} + n_i(t) \\ &= \sum_{d=1}^D u_d(t) e^{-j\pi i \sin \theta_d} + n_i(t) \quad i = 0, 1, 2, \dots, M - 1 \end{aligned} \quad (2.8)$$

Equation 2.8 is also usually written in a matrix form as:

$$\begin{aligned} \begin{bmatrix} x_0(t) \\ x_1(t) \\ \vdots \\ x_{M-1}(t) \end{bmatrix} &= \begin{bmatrix} 1 & 1 & \dots & 1 \\ e^{-j\pi \sin \theta_1} & e^{-j\pi \sin \theta_2} & \dots & e^{-j\pi \sin \theta_D} \\ \vdots & \vdots & \ddots & \vdots \\ e^{-j\pi(M-1) \sin \theta_1} & e^{-j\pi(M-1) \sin \theta_2} & \dots & e^{-j\pi(M-1) \sin \theta_D} \end{bmatrix} \begin{bmatrix} u_1(t) \\ u_2(t) \\ \vdots \\ u_D(t) \end{bmatrix} + \begin{bmatrix} n_0(t) \\ n_1(t) \\ \vdots \\ n_{M-1}(t) \end{bmatrix} \\ X_{M \times 1} &= A_{M \times D} U_{D \times 1} + N_{M \times 1} \end{aligned} \quad (2.9)$$

where  $A_{M \times D} = [a(\theta_1) \ a(\theta_2) \ \dots \ a(\theta_D)]$  is commonly called *array manifold* and the column  $a(\theta)$  is termed *steering vector* [SB08].

## 2.3 DOA Estimation Algorithms

There is a multitude of algorithms to estimate the DOA using signals received by an antenna array. In general they can be classified into two categories, namely spectral-based and parametric approach [KV96]. In this thesis we will concentrate on the spectral-based methods. The spectral-based methods can be divided into two categories, i.e. beamforming techniques and subspace-based methods.

### 2.3.1 Beamforming techniques

Beamforming techniques are among the earliest DOA estimation algorithms. The examples are classical beamforming (also known as Barlett) and MVDR beamforming [KV96]. In principle, the algorithms operate by scanning how much power is impinging on the antenna array from every direction. The angles with the highest power are determined as the DOA estimates.

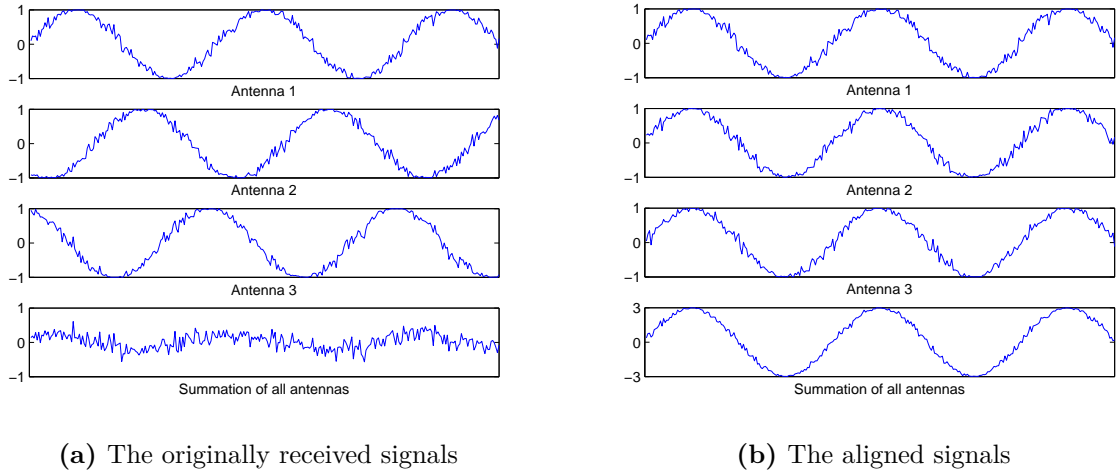
#### Classical Beamforming

In the phased-array technique, the signal received by each antenna element is a phase shifted version of that of the adjacent element. This fact leads to a simple and obvious solution to estimate the DOA of incoming signals, i.e. shifting the received signals such that all of them are perfectly aligned. The summation of the lined up signals will constructively result in a high value. This *delay and sum* mechanism is mathematically expressed as:

$$y(t) = w^H x(t) \tag{2.10}$$

where  $x(t)$  is the signal received by the antenna array,  $w$  is a weighting function that delays the received signals, and  $y(t)$  represents the *delay and sum* output. The weighting function  $w$  is chosen equal to the steering vector  $a(\theta)$  as in Equation 2.9. Figure 2.9 shows a simulation of a 3-element ULA receiving a noisy sinusoidal wave originating from a direction of  $45^\circ$ . Therefore, two adjacent antennas have a phase difference of  $127.27^\circ$  that is a result of shifting by  $e^{-j\pi \sin(45^\circ)}$  according to Equation 2.9. It is clearly shown that a direct summation of the original signals results in lower values than the ones with alignment.

Classical beamforming is, however, more commonly expressed in term of total aver-


**Figure 2.9:** Delay and sum mechanism

age power [ZCY10]:

$$\begin{aligned}
 P(\theta) &= \frac{1}{N} \sum \|y(t_n)\|^2 \\
 &= \frac{1}{N} \sum_{n=1}^N w^H(\theta) x(t_n) x^H(t_n) w(\theta) \\
 &= \frac{1}{N} \sum_{n=1}^N a^H(\theta) x(t_n) x^H(t_n) a(\theta) \\
 &= a(\theta)^H R a(\theta)
 \end{aligned} \tag{2.11}$$

where  $N$  is the number of snapshots, and  $R$  is the signal covariance matrix. Thus, Equation 2.11 is a problem of searching over all directions  $\theta$ , and the highest peaks are determined as the DOA estimates.

### MVDR beamforming

The Minimum Variance Distortionless Response (MVDR) beamforming has a similar idea like the classical beamforming in terms of searching for directions of arrival that have a maximum power. However, the MVDR imposes an additional constraint, that is keeping the response in the look direction constant (or distortionless) while at the same time minimizing the received power (or variance). This, in effect, suppresses the power from the remaining directions. Mathematically, this is described as the minimization of the received power with respect to the weighting function  $w$  [JeffreyFoutz2008]:

$$\min_w P(w) = \min_w E[\|y(t)\|^2] = \min_w w^H R w \quad \text{subject to } w^H a(\theta) = 1 \tag{2.12}$$

The solution to Equation 2.12 is obtained with a weighting function given by:

$$w = \frac{R^{-1}a(\theta)}{a^H(\theta)R^{-1}a(\theta)} \quad (2.13)$$

So the MVDR power spectrum is obtained as:

$$\begin{aligned} P_{MVDR} &= w^H R w \\ &= \frac{1}{a^H(\theta)R^{-1}a(\theta)} \end{aligned} \quad (2.14)$$

Figure 2.10 depicts the power spectrum of a signal from  $0^\circ$  that impinges on a six-element ULA. It can be seen that the power spectrum of the classical beamforming comes with sidelobes. In contrast, the MVDR power spectrum significantly minimize the sidelobes.

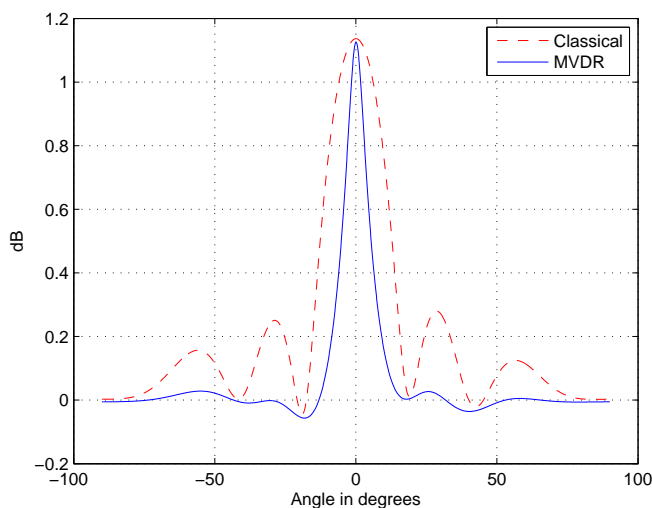


**Figure 2.10:** Power spectrum of the classical and MVDR beamforming

### 2.3.2 MUSIC algorithm

Taking a different approach, a subspace-based algorithm relies on the eigendecomposition of the signal covariance matrix. Technically, eigendecomposition of the signal covariance is meant to separate the signal subspace and the noise subspace, which are orthogonal to each other. The signal subspace is spanned by eigenvectors that correspond to the larger eigenvalues, whereas the noise subspace is spanned by eigenvectors of the smaller eigenvalues. The matrix of noise eigenvectors is defined as:

$$V_n = [q_{d+1}, \dots, q_M] \quad (2.15)$$

where  $d$  is the number of incoming signals, and  $M$  is the number of array elements. This means that the subspace-based algorithm requires the knowledge of the number of signals, which can be estimated using Minimum Descriptive Length (MDL) or Akaike Information Criteria (AIC) algorithm [Tre02].

An example of a subspace-based algorithm is the multiple signal classification (MUSIC) algorithm [Sch86] which makes use of noise subspaces. The key property exploited in the MUSIC algorithm is that the noise subspace and steering vector are orthogonal to each other. So, when the noise subspaces are projected onto steering vectors of the true DOAs, a result of zero (or approaching zero) will be obtained. Obviously, taking the inverse of these projection results will produce very high values. The problem is left as a one dimension search over DOAs that result in sharp peaks. The MUSIC algorithm is formally defined as:

$$P_{MUSIC}(\theta) = \frac{1}{\|a^H(\theta)V_n\|^2} = \frac{1}{a^H(\theta)V_nV_n^H a(\theta)} \quad (2.16)$$

Although the MUSIC algorithm is good at solving closely spaced signals, it still has a major limitation, i.e. the inability to deal with correlated signals. This is because signal and noise subspace separation using eigendecomposition relies on the full rank property of the signal covariance matrix. Whereas, correlated signals are linearly dependent to each other, and therefore the full rank property does not hold anymore.

## 2.4 Multipath Environments

In an ideal situation, there should only be a single signal component backscattered by the RFID tag, which travels through a straight path to the RFID reader's antenna. However in a practical environment, the presence of multipath components is not uncommon [Mol10]. These additional signals can be caused by reflection or diffraction of interacting objects in the surroundings, such as metal, windows, walls, etc. These signal replicas travel longer paths than the original one does, so they will have lower power when they arrive at the RFID reader's antenna. In other words, multipath signals are amplitude scaled and phase-shifted version of the original signal.

### Forward/Backward Spatial Smoothing

The presence of multipath signals is notorious in the failure of subspace based DOA estimation algorithms, such as MUSIC, ESPRIT, and their variants. Multipath signals are correlated to one another, and make the signal covariance become rank-deficient [ZCY10]. Consequently, eigendecomposition of the signal covariance fails to split the signal and noise subspaces. Therefore, for example the MUSIC algorithm,

which relies on noise subspaces in the spectrum scanning, will give incorrect DOA estimations.

Shan *et al.* [SWK85] have shown that *spatial smoothing* pre-processing can restore the rank of correlated signal covariance. The idea is to divide the antenna array into multiple overlapping subarrays and to take the average of their covariance matrices. It has been proved that spatial smoothing pre-processing can help the MUSIC algorithm to estimate the DOA of correlated signals correctly. However spatial smoothing requires a considerably larger number of antenna elements. To solve  $K$  number of correlated signals, at least  $2K$  antennas are needed, whereas the conventional MUSIC algorithm only requires  $K + 1$  antennas.

In an attempt to reduce the required number of antennas, Pillai and Kwon [PK89] proposed an improved spatial smoothing technique, which is called forward/backward spatial smoothing (FBSS). They suggest that FBSS only demands  $3K/2$  antennas to solve  $K$  correlated signals. FBSS makes use of Evan's spatial smoothing, which is called forward smoothing, and additional backward smoothing at the same time.

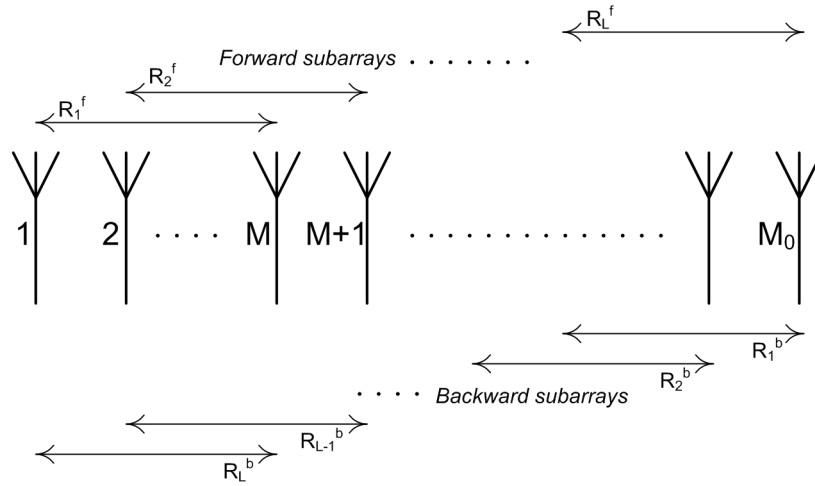


**Figure 2.11:** Forward/backward subarrays

### Forward subarrays

Let there be  $K$  narrow-band correlated signals impinging at  $M_0$  elements uniform of the linear array from direction  $\theta_1, \theta_2, \dots, \theta_k$ . These correlated signals  $u_1(t), u_2(t), \dots, u_k(t)$  are scaled and phase-shifted versions of each other. Assume  $u_1(t)$  is the signal traveling through the straight line of sight (LOS), thus the other signals are the attenuated version, and can be modelled as:

$$u_k(t) = \alpha_k u_1(t) \quad k = 1, 2, \dots, K \quad (2.17)$$

where  $\alpha_k$  denotes the complex attenuation of the  $k$ th signal with regard to the first signal  $u_1(t)$ .

In the case of a half-wavelength spaced uniform linear array (ULA),  $x_i(t)$  the signal received at each antenna element at time  $t$  is modelled as:

$$x_i(t) = \sum_{k=1}^K u_k(t) e^{(-j\pi(i-1)\sin\theta_k)} + n_i(t) \quad i = 1, 2, 3, \dots, M_0 \quad (2.18)$$

where  $n_i(t)$  is zero mean and uncorrelated noise present at the  $i$ th antenna.

As shown in Figure 2.11  $M_0$  antenna elements are splitted into  $L$  forward subarrays where each consists of  $M$  elements. According to the conventional method, where the signals are uncorrelated and the array is not divided into smaller arrays, the number of array elements must be greater than the number of impinging signals,  $M \geq K + 1$ . Let  $x_l^f(t)$  denote the signals received at the  $l$ th forward subarray:

$$x_l^f(t) = [x_l(t) \quad x_{l+1}(t) \quad \dots \quad x_{l+M-1}(t)]^T \quad 1 \leq l \leq L \quad (2.19)$$

and its covariance matrix is defined as:

$$R_l^f = E[x_l^f(t) (x_l^f(t))^H] \quad (2.20)$$

where  $E[\cdot]$  is the expected value and  $(\cdot)^H$  is conjugate transpose (also called Hermitian). Therefore taking the average covariance of  $L$  forward subarrays yields:

$$R^f = \frac{1}{L} \sum_{l=1}^L R_l^f \quad (2.21)$$

If there are  $M_0$  elements in total, then  $M_0 - M + 1$  sets of subarrays can be formed. To solve  $K$  correlated signals, at least  $K$  sets of subarrays are required [SWK85]. Therefore,

$$\begin{aligned} M_0 - M + 1 &\geq K \\ M_0 - (K + 1) + 1 &\geq K \\ M_0 &\geq 2K \end{aligned} \quad (2.22)$$

### Backward subarrays

Using forward subarrays solely requires at least  $2K$  antennas to solve  $K$  correlated signals. Pillai and Kwon extend the idea of forward smoothing by exploiting  $L$  backward subarrays as well. Let  $x_l^b(t)$  be the *complex conjugate* of the signals received at the  $l$ th backward subarray:

$$x_l^b(t) = [x_{M_0-l+1}^*(t) \quad x_{M_0-l}^*(t) \quad \dots \quad x_{L-l+1}^*(t)]^T \quad 1 \leq l \leq L \quad (2.23)$$

and the covariance matrix is defined as:

$$R_l^b = E \left[ x_l^b(t) (x_l^b(t))^H \right] \quad 1 \leq l \leq L \quad (2.24)$$

Therefore taking the average covariance of  $L$  backward subarrays yields:

$$R^b = \frac{1}{L} \sum_{l=1}^L R_l^b \quad (2.25)$$

Finally the new FBSS covariance is obtained as the average of the forward and backward subarrays:

$$\tilde{R} = \frac{R^f + R^b}{2} \quad (2.26)$$

In FBSS scheme, the total number of elements  $M_0$  can be formed into  $2(M_0 - M + 1)$  sets of subarrays. Recall that to solve  $K$  correlated signals, at least  $K$  sets of subarrays, with each consists of at least  $K + 1$  elements, are required. Therefore,

$$\begin{aligned} 2(M_0 - M + 1) &\geq K \\ 2M_0 - 2(K + 1) + 2 &\geq K \\ M_0 &\geq 3K/2 \end{aligned} \quad (2.27)$$

So using at least  $3K/2$  antennas, FBSS pre-processing can help subspace-based algorithms, like MUSIC, to solve  $K$  correlated signals.

### Efficacy of FBSS

If there are  $K$  *uncorrelated* signals impinging on  $M$  (at least  $K + 1$ ) antennas, the received signal covariance matrix will have a *rank* of  $\min(K, M) = K$ , which means that the covariance matrix is made up of  $K$  independent rows or columns. Note that this is assuming the absence of noise in order to clearly show the relation between signal correlation and matrix rank. Of course in the presence of noise, the covariance matrix will have a rank  $M$ , but the noise is somewhat concealing the true signal rank. Eigendecomposition of the rank  $K$  covariance matrix will result in  $K$  large eigenvalues and  $M - K$  zero eigenvalues. The  $K$  large eigenvalues correspond to eigenvectors that span the *signal subspace*, whereas the  $M - K$  eigenvectors span the *noise subspace* [SWK85]. The signal and noise subspaces separation is a crucial step for the success of the MUSIC algorithm because the algorithm is based on the noise subspace.

However, if the  $K$  signals are *correlated*, the covariance matrix rank will be less than  $K$ . For example, if they are all correlated, the rank of the covariance matrix becomes one, as the signals are all dependent on each other. Note, this is again assuming the

absence of noise. Therefore, eigendecomposition of the covariance matrix will result in only a single large eigenvalue and  $M - 1$  zero eigenvalues. This is known as the root cause of the failure of subspace based algorithms like MUSIC.

What FBSS actually does is restoring the rank deficiency of correlated covariance matrices. The comprehensive mathematical proofs can be found in [PK89]. Here, a simple example is discussed to analyze how the forward spatial smoothing algorithm works. Let there be two correlated signals  $k_1$  and  $k_2$  from direction  $\theta_1$  and  $\theta_2$  impinging on a four-element ULA. Because there are two correlated signals, two sets of subarray which each consists of three elements, are needed. Therefore the four-element ULA will be formed into two sets of forward subarrays. The noiseless signals received at the first subarray  $x_{13}$ :

$$\begin{aligned} x_{13} &= \begin{pmatrix} e^0 k_1 + e^0 k_2 \\ e^{-j\sin\theta_1} k_1 + e^{-j\sin\theta_2} k_2 \\ e^{-2j\sin\theta_1} k_1 + e^{-2j\sin\theta_2} k_2 \end{pmatrix} \\ &= \begin{pmatrix} e^0 & e^0 \\ e^{-j\sin\theta_1} & e^{-j\sin\theta_2} \\ e^{-2j\sin\theta_1} & e^{-2j\sin\theta_2} \end{pmatrix} \begin{pmatrix} e^0 & 0 \\ 0 & e^0 \end{pmatrix} \begin{pmatrix} k_1 \\ k_2 \end{pmatrix} \\ &= A \begin{pmatrix} e^0 & 0 \\ 0 & e^0 \end{pmatrix} \begin{pmatrix} k_1 \\ k_2 \end{pmatrix} \end{aligned}$$

whereas the signals received at the second subarray  $x_{24}$  is expressed as:

$$\begin{aligned} x_{24} &= \begin{pmatrix} e^{-j\sin\theta_1} k_1 + e^{-j\sin\theta_2} k_2 \\ e^{-2j\sin\theta_1} k_1 + e^{-2j\sin\theta_2} k_2 \\ e^{-3j\sin\theta_1} k_1 + e^{-3j\sin\theta_2} k_2 \end{pmatrix} \\ &= \begin{pmatrix} e^0 & e^0 \\ e^{-j\sin\theta_1} & e^{-j\sin\theta_2} \\ e^{-2j\sin\theta_1} & e^{-2j\sin\theta_2} \end{pmatrix} \begin{pmatrix} e^{-j\sin\theta_1} & 0 \\ 0 & e^{-j\sin\theta_2} \end{pmatrix} \begin{pmatrix} k_1 \\ k_2 \end{pmatrix} \\ &= A \begin{pmatrix} e^{-j\sin\theta_1} & 0 \\ 0 & e^{-j\sin\theta_2} \end{pmatrix} \begin{pmatrix} k_1 \\ k_2 \end{pmatrix} \end{aligned}$$

Therefore the averaged covariance matrix  $\tilde{R} = (x_{13}x_{13}^H + x_{24}x_{24}^H)/2$ . Now the task is to show that  $\tilde{R}$  has a rank of two. It is clear that the array manifold  $A$  always has a rank equal to the number of signals, so it can be left out to simplify the analysis.

Then by ignoring the denominator as well, the modified  $\tilde{R}$  becomes  $\hat{R}$  :

$$\begin{aligned}\hat{R} &= \begin{pmatrix} e^0 & 0 \\ 0 & e^0 \end{pmatrix} \begin{pmatrix} k_1 \\ k_2 \end{pmatrix} \begin{pmatrix} k_1 \\ k_2 \end{pmatrix}^H \begin{pmatrix} e^0 & 0 \\ 0 & e^0 \end{pmatrix}^H + \\ &\quad \begin{pmatrix} e^{-j\sin\theta_1} & 0 \\ 0 & e^{-j\sin\theta_2} \end{pmatrix} \begin{pmatrix} k_1 \\ k_2 \end{pmatrix} \begin{pmatrix} k_1 \\ k_2 \end{pmatrix}^H \begin{pmatrix} e^{-j\sin\theta_1} & 0 \\ 0 & e^{-j\sin\theta_2} \end{pmatrix}^H \\ &= \left[ \begin{pmatrix} e^0 & 0 \\ 0 & e^0 \end{pmatrix} \begin{pmatrix} k_1 \\ k_2 \end{pmatrix} \quad \begin{pmatrix} e^{-j\sin\theta_1} & 0 \\ 0 & e^{-j\sin\theta_2} \end{pmatrix} \begin{pmatrix} k_1 \\ k_2 \end{pmatrix} \right] \\ &\quad \left[ \begin{pmatrix} e^0 & 0 \\ 0 & e^0 \end{pmatrix} \begin{pmatrix} k_1 \\ k_2 \end{pmatrix} \quad \begin{pmatrix} e^{-j\sin\theta_1} & 0 \\ 0 & e^{-j\sin\theta_2} \end{pmatrix} \begin{pmatrix} k_1 \\ k_2 \end{pmatrix} \right]^H \\ &= DD^H\end{aligned}$$

So it is necessary to show that  $D$  has a rank of two:

$$\begin{aligned}D &= \left[ \begin{pmatrix} e^0 & 0 \\ 0 & e^0 \end{pmatrix} \begin{pmatrix} k_1 \\ k_2 \end{pmatrix} \quad \begin{pmatrix} e^{-j\sin\theta_1} & 0 \\ 0 & e^{-j\sin\theta_2} \end{pmatrix} \begin{pmatrix} k_1 \\ k_2 \end{pmatrix} \right] \\ &= \begin{bmatrix} e^0 k_1 & e^{-j\sin\theta_1} k_1 \\ e^0 k_2 & e^{-j\sin\theta_2} k_2 \end{bmatrix} \\ &= \begin{bmatrix} k_1 & 0 \\ 0 & k_2 \end{bmatrix} \begin{bmatrix} e^0 & e^{-j\sin\theta_1} \\ e^0 & e^{-j\sin\theta_2} \end{bmatrix}\end{aligned}$$

It is clear that  $D$  indeed has a rank of two if  $\theta_1 \neq \theta_2$ , and therefore the averaged covariance matrix  $\tilde{R}$  also has a rank of two. This rank restoration helps the MUSIC algorithm to solve correlated signals correctly.

Figure 2.12 shows an example of the efficacy of FBSS preprocessing to assist the MUSIC algorithm in estimating correlated signals correctly. A six-element ULA receives four correlated signals originating from  $-45^\circ$ ,  $-20^\circ$ ,  $10^\circ$ , and  $30^\circ$ , each with an SNR of 5 dB. It is shown that the FBSS smoothed signals result in sharp peaks at the true DOAs, while it is not the case without such preprocessing.

Despite its high resolution characteristic, at some point the MUSIC algorithm can also fail to solve closely spaced signals. It was found that with a six-element ULA, FBSS MUSIC cannot solve correlated signals that are less than  $10^\circ$  spaced. Figure 2.13 illustrates the MUSIC spectrum of a six-element ULA receiving four signals coming from  $-45^\circ$ ,  $-20^\circ$ ,  $20^\circ$ , and  $30^\circ$ . Although the FBSS MUSIC produces very high peaks, the closely spaced signals are not determined correctly.

In reflective environments, a single signal source usually comes with its multipath components. If the signal line of sight (LOS) is available, then the true DOA will have the highest power since the multipath components travel longer paths and will consequently lose more power. Sometimes, we are only interested in the true signal source, and it can be determined if each signal's power is known.

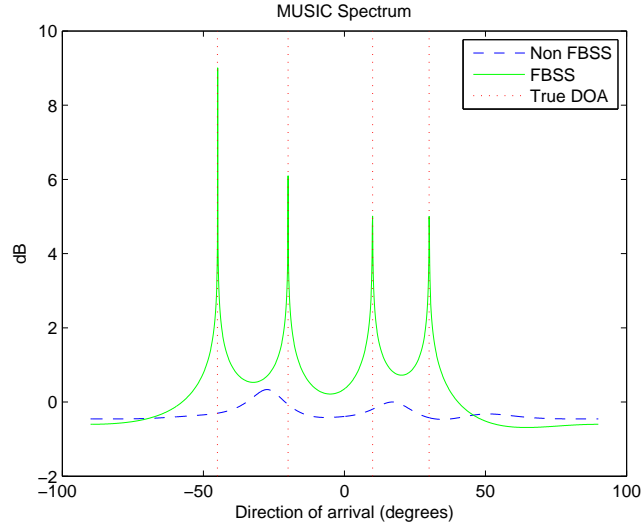


**Figure 2.12:** MUSIC spectrum of a six-element ULA receiving four correlated signals with power of 5 dB originating from  $-45^\circ$ ,  $-20^\circ$ ,  $10^\circ$ , and  $30^\circ$

The peak values of MUSIC power spectrum generally do not correspond with the actual power. The highest peak in the spectrum is not necessarily the one having the highest power. Instead, the actual power can be computed as follows. Given the signal model  $X = AU + N$  as in Equation 2.9, the signal covariance matrix is expressed as:

$$\begin{aligned}
 R &= [XX^H] \\
 &= A[UU^H]A^H + [NN^H] \\
 &= APA^H + \lambda I
 \end{aligned} \tag{2.28}$$

where  $\lambda$  is a scalar value calculated from the average of noise eigenvalues,  $I$  is the identity matrix, and diagonal elements of matrix  $P$  are the signals' power. So, if the DOAs are already found, the array manifold  $A$  can be constructed. Therefore, using Moore-Penrose pseudo-inverse, eventually  $P$  can be computed as [Sch86]:

$$P = (A^H A)^{-1} A^H (R - \lambda I) A (A^H A)^{-1} \tag{2.29}$$

## 2.5 Number of Signals Detection

Estimation of how many signal components that are received at the antenna array is a critical step because many DOA estimation algorithms rely on it. Several methods have been proposed to address the signal detection problem. Xin *et al.* [XZS07] briefly summarize the existing methods into two categories, i.e. parametric and non-parametric methods. Parametric methods such as Maximum Likelihood Estimation

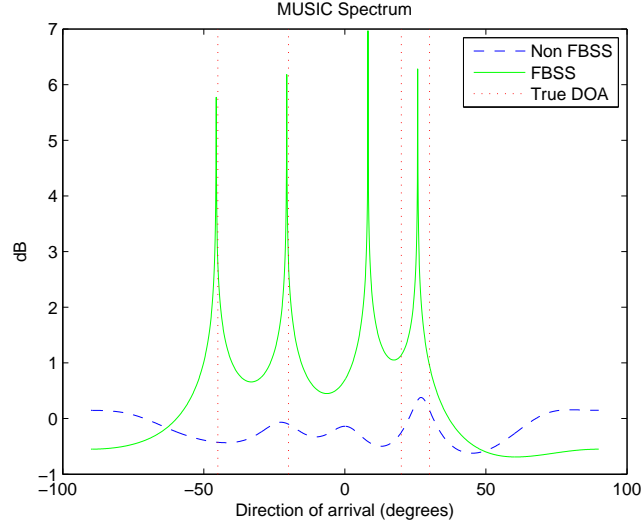


**Figure 2.13:** MUSIC spectrum of a six-element ULA receiving four correlated signals with power of 10 dB originating from  $-45^\circ$ ,  $-20^\circ$ ,  $20^\circ$ , and  $30^\circ$

(MLE) generally performs well even in multipath environments. Unfortunately MLE requires prohibitively high computation loads. In the non-parametric category, the Akaike information criterion (AIC) and the minimum description length (MDL) are the most well-known and are very attractive from a computation perspective [XZS07]. These algorithms are based on the fact that normally eigendecomposition of the signal covariance matrix will result in a cluster of *smaller* eigenvalues which represent the noise, whereas the number of *bigger* eigenvalues are equal to the number of signals. However, under multipath environments this is not true because a correlated covariance matrix is rank deficient. Consequently, the number of bigger eigenvalues will be lower. In such a situation, FBSS preprocessing should be employed before applying the AIC or MDL algorithm.

## MDL and AIC algorithms

The MDL algorithm is implemented by varying the number of signals  $d \in \{0, 1, 2, \dots, M-1\}$  in order to minimize the following function [Tre02]:

$$MDL(d) = N(M-d) \ln \left\{ \frac{\frac{1}{M-d} \sum_{i=d+1}^M \lambda_i}{\left( \prod_{i=d+1}^M \lambda_i \right)^{\frac{1}{M-d}}} \right\} + p(d) \quad (2.30)$$

where  $M$  is the number of antennas, and  $N$  is the number of samples, and  $\lambda$  is a vector of descending ordered eigenvalues.  $p(d)$  is a penalty function which is defined differently between a plain and FBSS covariance matrix:

$$p(d) = \frac{1}{2}(d(2M-d) + 1) \ln N \quad (2.31)$$

$$p(d)_{FBSS} = \frac{1}{4}d(2M - d + 1)\ln N \quad (2.32)$$

The first term of the MDL algorithm is a log-likelihood function which decreases as the  $d$  increases. However the second term, i.e. the penalty function increases together with  $d$ . This results in a behavior that the MDL will decrease as  $d$  increases, and start to rebound when  $d$  is higher than the actual signal counts. So,  $d$  that minimizes the MDL is determined as the number of signals.

The AIC algorithm has a similar notion like MDL, except that the penalty function is different [Tre02]:

$$p(d) = d(2M - d) \quad (2.33)$$

$$p(d)_{FBSS} = \frac{1}{2}d(2M - d + 1) \quad (2.34)$$

The MDL algorithm is said to have more consistent estimations than AIC when a large number of samples are available [Tre02].

Figure 2.14 shows a simulation of MDL and AIC. There are three correlated signals with SNR 5 dB originating from  $-10^\circ$ ,  $0^\circ$ , and  $10^\circ$  impinging on a six-element ULA. The received data is decorrelated using FBSS before fed to MDL and AIC. It can be seen that the MDL and AIC algorithm successfully estimate the number of signals, which is indicated by the their lowest value with a signal count of 3.

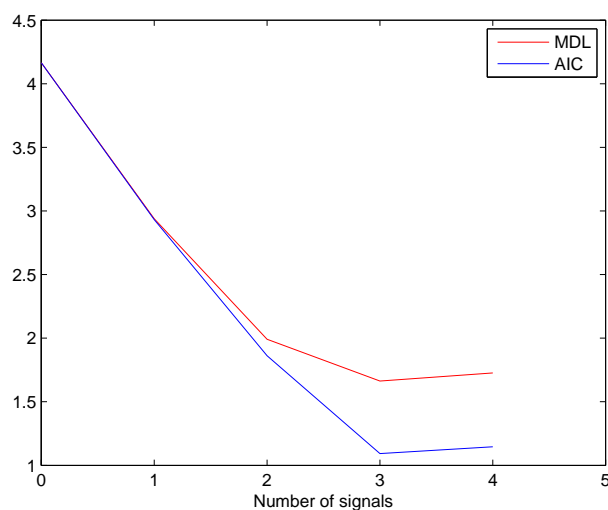
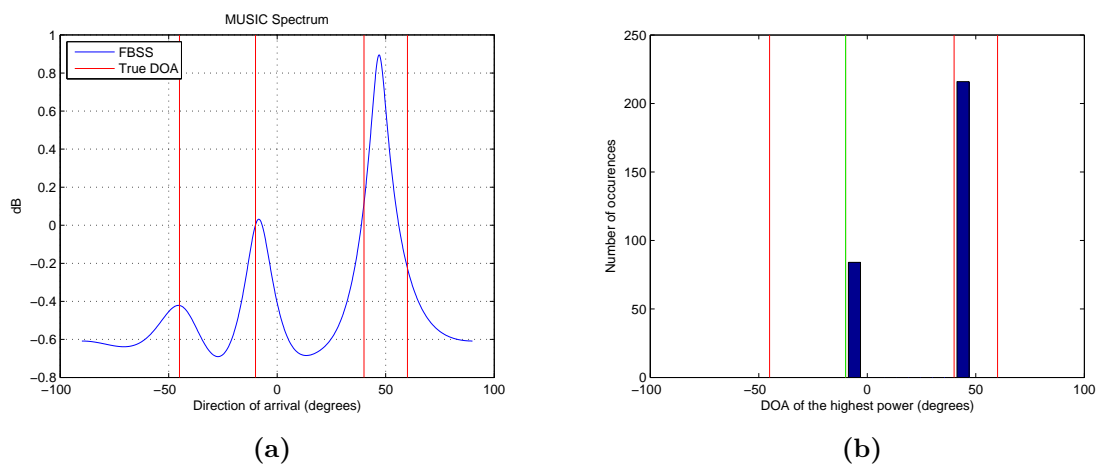


**Figure 2.14:** MDL and AIC correctly detect the presence of three signals

## 2.6 Underestimating vs Overestimating Number of Signals

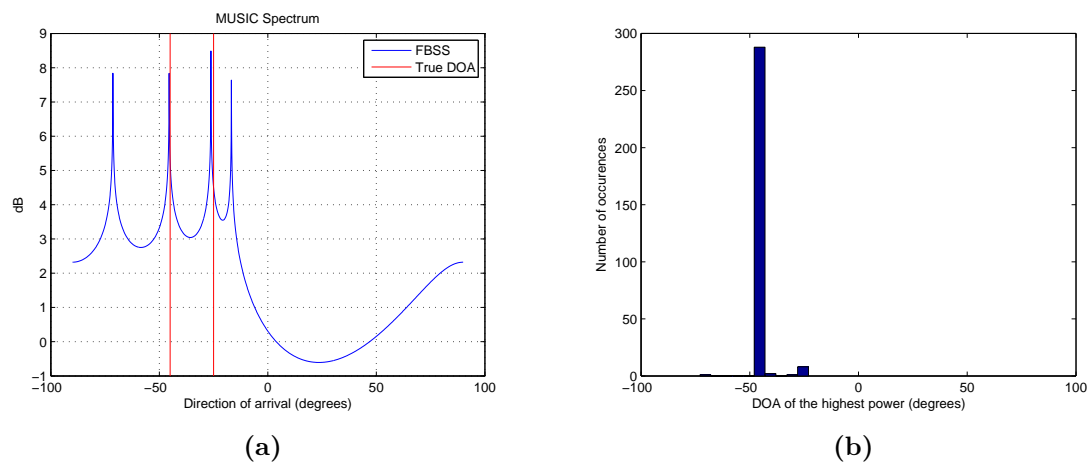
There are numerous factors than can affect the performance of MDL and AIC, for example signal strengths, signal separations, correlation, and number of samples. A false detection of signal counts can be either underestimation or overestimation.

Figure 2.15 shows simulation results of signal counts underestimation. There are four correlated signals coming from  $-45^\circ$ ,  $-10^\circ$ ,  $40^\circ$ , and  $60^\circ$  with correlation constants  $(1+0i)$ ,  $(0.8+1i)$ ,  $(0.8-0.4i)$ , and  $(0.6+0.3i)$ , respectively. These signals impinge on a 6-element ULA. The presence of four signals is deliberately underestimated as two signals. It can be seen that distantly separated signals can still be detected correctly, whereas closely spaced ones tend to blend together and appear as a single peak with their aggregated powers. This simulation is run for 300 times. In each simulation the highest power DOA among several detected DOAs is recorded. Figure 2.15b shows the occurrence of the highest power DOA in those 300 simulations. According to the signal model, the signal from  $-10^\circ$  is the one having the highest power. However, signals from  $40^\circ$  and  $60^\circ$  appear to be mixed up and their combined powers become apparently higher than the one from  $-10^\circ$ .



**Figure 2.15:** Number of signals underestimation

To examine the effect of overestimation, simulations are also done. Two correlated signals originating from  $-45^\circ$  and  $-25^\circ$  with correlation factor  $(1+0i)$  and  $(0.6+0.5i)$  impinge on a 6-element ULA. The number of signals is intentionally overestimated as four. Indeed, the MUSIC spectrum shows four sharp peaks, where two peaks correspond to the true DOAs and the others are spurious peaks. Figure 2.16b depicts the occurrence of the strongest power DOA in 300 simulations. In general, the actual strongest DOA, i.e. near  $-45^\circ$  can be determined correctly. Yet, some wrong detections at  $-25^\circ$  are unavoidable. Spurious peaks around  $-70^\circ$  are also occasionally chosen as the highest power DOA.



**Figure 2.16:** Number of signals overestimation



# 3 Implementation

## 3.1 Applicability of phased-array to Gen 2 UHF RFID

In previous sections, the operation principles of a phased-array and the communication protocols of Gen 2 UHF RFID have been described. However at this point the applicability of phased-array to determine the Gen 2 tag's DOA is not assessed yet.

One of the criteria in the phased-array technique is that the arriving signal should be a narrowband signal, which means the baseband waveform is not varying by much while the signal is traveling across the array structure. Technically speaking, the inverse of baseband bandwidth should be much larger than the signal propagation time. With an operating frequency of 866 MHz, the UHF RFID system has a wavelength of 34 cm. Let's say the phased-array is a half-wavelength spaced 6-element ULA, then the array has a length of around 1 meter. Therefore, it takes at most  $1/(3 \times 10^8) = 3.3 \times 10^{-9}$  s for the tag's signal to travel across the array. On other hand, a tag is typically operating on a BLF of 250 kHz. So the inverse of the bandwidth is  $1/(250 \times 10^3) = 4 \times 10^{-6}$  s, which is indeed much greater than the propagation time  $3.3 \times 10^{-9}$  s.

Another criterion is the far-field assumption. Again, assuming the ULA has a length of 1 meter, according to Equation 2.1 the far-field assumption is satisfied if the distance between the tag and the array is larger than  $2D^2/\lambda = 2 \cdot 1^2/0.34 = 5.88$  meter. In fact, the operation range of Gen 2 UHF RFID is usually less than 5 meter. Consequently, some inaccuracies are expected in the estimated DOAs. It is shown in [vL13] that the MUSIC algorithm can be modified to work on near-field mode. However, it is not employed in this research.

## 3.2 Hardware implementation

The previous implementation consists of a four-element antenna array [vL13]. In the current one, it is extended to six-element antennas. The antenna being used is a patch antenna. The antenna is circularly polarized, so that regardless of the tag orientation the antenna can still read the tag.

The antenna elements are half wavelength apart, measured from the center point of the patches. Like typical patch antenna, they are mounted on ground planes. In addition to this six-element array, there is also a patch that is dedicated to the

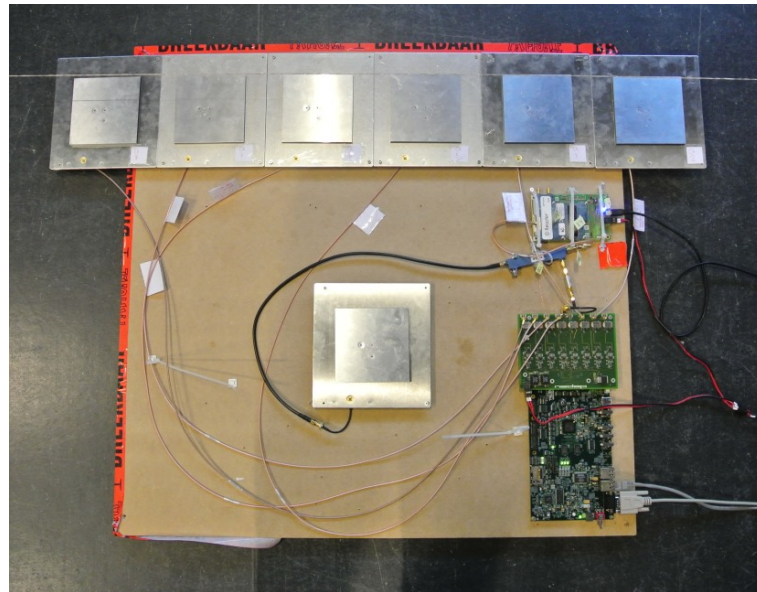


**Figure 3.1:** Photograph of the setup

off-the-shelf RFID reader operating in monostatic mode, where a single antenna is used for both transmitting and receiving signals.

By default the RFID reader works on frequency-hopping mode in order to reduce interference effects from other nearby readers. Altering this default operation is not desirable. On other hand, for the downmixers to work correctly, they should somehow have a local oscillator that is synchronized with the reader's frequencies at any time. The fact that the reader keeps transmitting continuous waves while listening to the tag response can be used to source the downmixer's local oscillator. It is implemented by tapping the reader's antenna line via a directional coupler and an attenuator to dampen its strong power.

At the forefront of the analog processing board (Figure 3.2), a filter is used to pass only ETSI UHF RFID frequencies (865-868 MHz). Then the signals are downmixed to baseband in IQ format. With a baseband BLF of 250 kHz, the ADC sampling rate should be at least 500 kHz. Normally, a signal should be low pass filtered before it is digitized by ADC in order to prevent frequency aliasing. However such filter is not present in the board. To mitigate this situation, the ADC sampling rate is chosen specifically at 1.2 MHz. A more detailed explanation about this strategy can be found in [vL13]. The output from the ADC is fed to the OMAP-L137 DSP processor (Spectrum Digital EVMOMAPL137 evaluation board) and digitally filtered in order to suppress undesired frequency components that are still present because of the aliasing effects. For storing and further analysis, the data can be sent to a computer.

The RFID reader being used is an Impinj Indy R2000. It is configured to transmit at a power level of 30 dBm (1 watt). Moreover, it is set to output two digital

triggers, namely *Read Start* and *Read OK*. The former gives an indication that a tag starts sending its EPC. So the digital signal processor can start sampling the data. The latter gives information about the validity of the tag response just read. An invalid tag response can be caused by an extremely low tag SNR, strong multipath signals, or multiple tags responding at the same time. When the tag response is not decodable anymore by the RFID reader, it should be discarded by the digital signal processor as well. In each detected tag response, the signal processor takes 2048 samples within 1.7 ms. The tag itself is configured to use a Miller modulation and a BLF of 250 kHz. It takes 2.5 ms to send the electronic product codes (EPC) to the reader.

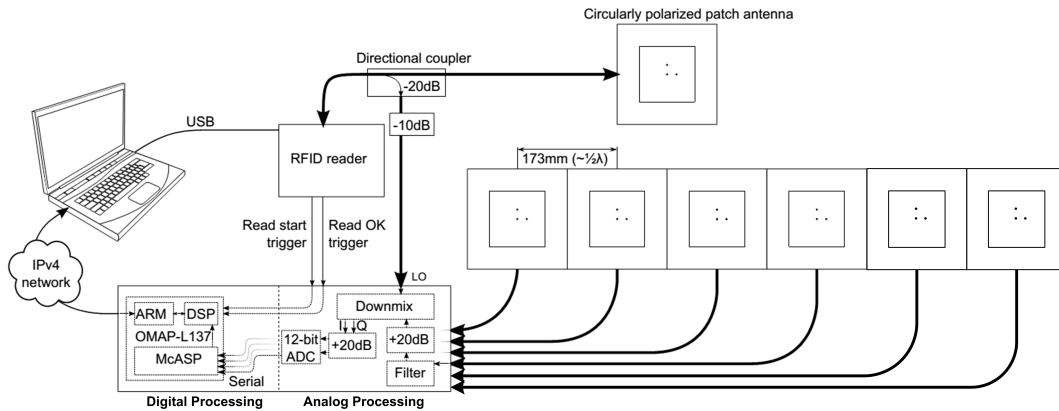


Figure 3.2: Block diagram of the hardware implementation[vL13]

## Phased-Array Calibration

From a hardware point of view, the uniformity of components in each channel is a crucial aspect that affects the DOA estimation accuracy in the phased-array technique. Electromagnetic waves received by the phased-array travel through antennas, cables, and a series of electronic components before they are finally converted to digital IQ data ready for *in silico* analysis.

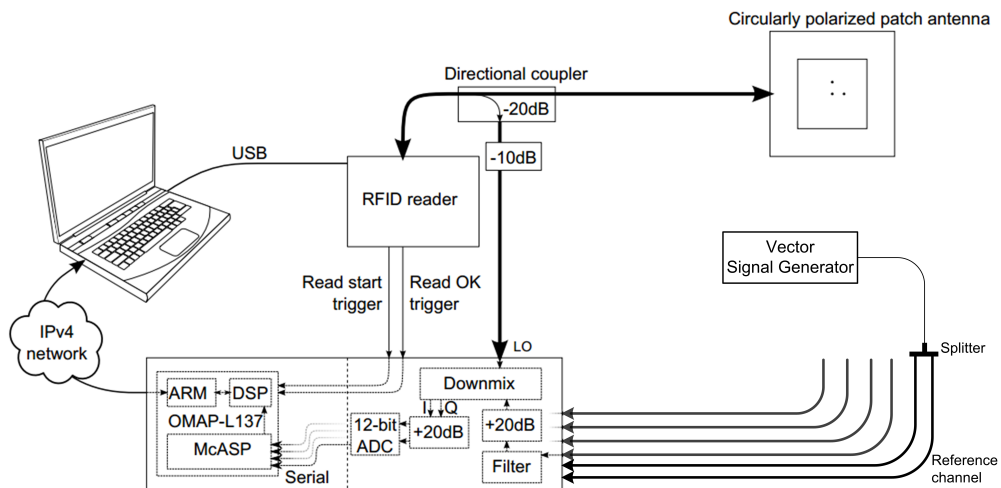
In DC or low frequency systems with wavelengths more than 1 km, cabling is only considered as the conductor of electrical signals and does not have significant impact on the systems. On the contrary, when the wavelength is less than 1 meter like in UHF systems, the cable length does have impact on the systems. The speed of electromagnetic propagation in coaxial cables is typically 2/3 of the speed of light [DS13]. So, the wavelength of an 866 MHz UHF RFID in coaxial cables is about 22.6 cm. This means even 1 cm difference in the cable length between two channels will result in  $(1/22.6) \times 360^\circ = 16^\circ$  of phase shift. Furthermore, the electrical signals must undergo several stages of processing, like filtering, amplification, mixing, and digitization until it becomes digital IQ data. The fact that every electronic component inherently has some deviation from its nominal value introduces non-uniform

responses among the channels. In the end, these inhomogeneities may accumulate to be a significant phase and magnitude response mismatch.

Therefore, to compensate the effect of non-uniformity, calibration is required. Ideally, the calibration should take all hardware parts into account, i.e. the antennas, cables, and electronic components involved in signal conditioning and digitization. In practice, this can be done by transmitting a single signal source from a far-field distance at the center of the antenna array. By doing so, the IQ constellations of all channels should align perfectly. Otherwise, corrections are required.

To ensure that there is only one signal source impinging on the antenna array, the calibration is desirably done in an anechoic chamber. But since the facilities were not available at hand, it was decided to assume that all of the antennas have identical responses. This assumption may be one of the contributing factors in the systematic error that will be reported in section 4.3.

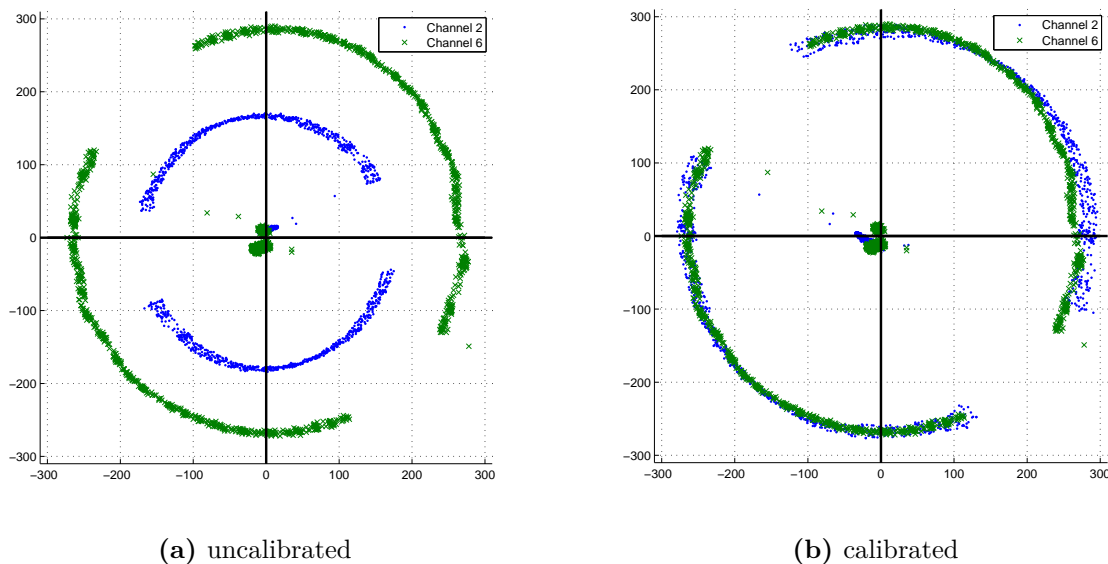
Figure 3.3 shows the calibration setup. The antenna array is not included. The vector signal generator (VSG) was set to generate a 250 kHz square wave modulated with RF 865.7 MHz, which is similar to the tag-to-reader signal. By default, the RFID reader is operating on frequency-hopping mode. Since the reader's local oscillator will be used to downmix the signal generated by the VSG, the reader and the VSG should operate at the same frequency. Therefore, for calibration purposes the reader was set to a fixed-frequency mode, i.e at 865.7 MHz. As a side note, since there was only one piece of a two-way splitter ready at hand, a pragmatic solution is taken, that is calibrating each channel individually against a reference channel.



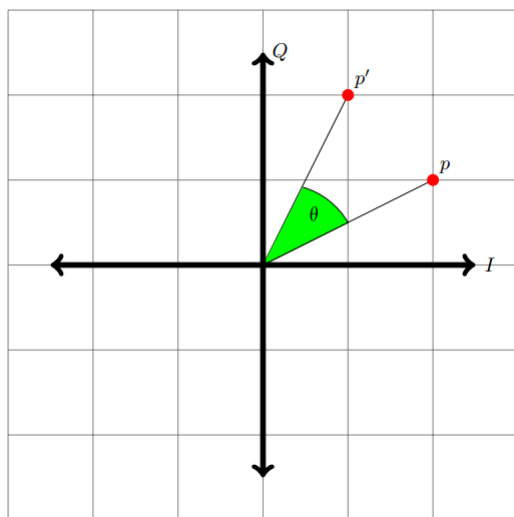
**Figure 3.3:** Calibration setup

Figure 3.4 depicts the IQ constellation of 2048 sampling points of Channel 2 and Channel 6. Instead of resembling a pair of spots like that of Binary Phase-Shift Keying, the constellation appears as a pair of arcs. This is due to the fact that the

RFID reader and the VSG have their own local oscillator, and thus some degree of frequency mismatch will occur. It explains why the IQ constellation seems to be rotating. Furthermore, Figure 3.4a clearly shows that there is a response discrepancy between Channel 2 and Channel 6. So corrections in terms of phase shift and magnitude multiplication are required.



**Figure 3.4:** IQ constellation of Channel 2 and Channel 6, pre and post calibration



**Figure 3.5:** Point rotation

A point  $p(i, q)$  that rotates by  $\theta$  angle counterclockwise to a new point  $p'(i', q')$  as

shown in Figure 3.5 can be described by a rotation matrix [Mat]:

$$\begin{pmatrix} i' \\ q' \end{pmatrix} = \begin{pmatrix} \cos\theta & -\sin\theta \\ \sin\theta & \cos\theta \end{pmatrix} \begin{pmatrix} i \\ q \end{pmatrix} \quad (3.1)$$

Therefore, if  $p$  and  $p'$  are given, then the angle of rotation can be computed as

$$\theta = \arctan\left(\frac{\sin\theta}{\cos\theta}\right) \quad (3.2)$$

where  $\sin\theta = (iq' - i'q) / (i^2 + q^2)$  and  $\cos\theta = (ii' + qq') / (i^2 + q^2)$ . The sign of  $\sin\theta$  and  $\cos\theta$  jointly indicate the extent of the rotation, whether it is within quadrant I, II, III, or IV.

Equation 3.2 was used to compute the value of correction for each pair of sample points in Channel 2 and Channel 6, and the final value was obtained by averaging the results from all points. Of course, before applying Equation 3.2 the magnitude of the two points being calibrated should be made equal. Figure 3.4b shows the IQ constellation after correction was applied.

The correction values for all channels, where Channel 6 is used as the reference, are shown in Table 3.1. Channel 1 and Channel 2 have significantly different correction values because the antenna cable length was shorter than that of other channels.

**Table 3.1:** Calibration constants with Channel 6 used as the reference

	Ch 1	Ch 2	Ch 3	Ch 4	Ch 5	Ch 6
Phase	130.8°	130°	332.6°	334°	340°	0
Magnitude	1.59	1.6	1.45	1.34	1.1	1

## 4 Measurements and Analysis

Measurements were carried out in various types of environments. To examine the system's performance under near-ideal situation where reflections are minimum, the experiments were done in a large room, SmartXP Lab at University of Twente. While for testing the performance in a reflection-rich environment comparable to retail shops, the experiments were done in several locations in the Zilverling office building at University of Twente. In a real deployment, the setup is designed to be placed on ceilings, but for ease of testing it was placed on the floor and the tag was hung on a string above the phased array. The tag was positioned at several heights starting from 100 cm and upward. It was found that with transmit power 30 dBm, the reader could only read the tags at the height up to 225 cm. At each height, the tag was moved horizontally along the string at an interval of 5 cm until it was not detectable anymore by the reader. For each horizontal position, 150 observations (tag read) were collected. And each observation consisted of 2048 samples which means a duration of 1.7 ms. Figure 4.1 illustrates the measurement setup.

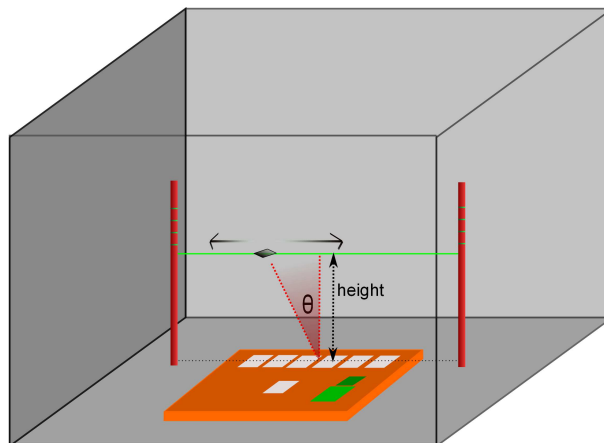


**Figure 4.1:** Measurement setup

Figure 4.2 depicts a typical IQ constellation of the received data. If the waveform is a perfect squarewave, then the constellation will form a pair of spot clouds around the coordinate center. Instead, it has a line-shaped cloud which can be viewed as distorted squarewave with changing amplitude. However, most importantly is that the *line* has a clear orientation.

Figures like in Figure 4.5 show the histograms of estimated DOAs at each tag's horizontal position. Every single patch represents a bin of  $3^\circ$  wide. The color of the

patch indicates the percentage of DOA estimations that fall within that bin. So, the total percentage at each horizontal position equals to 100%.

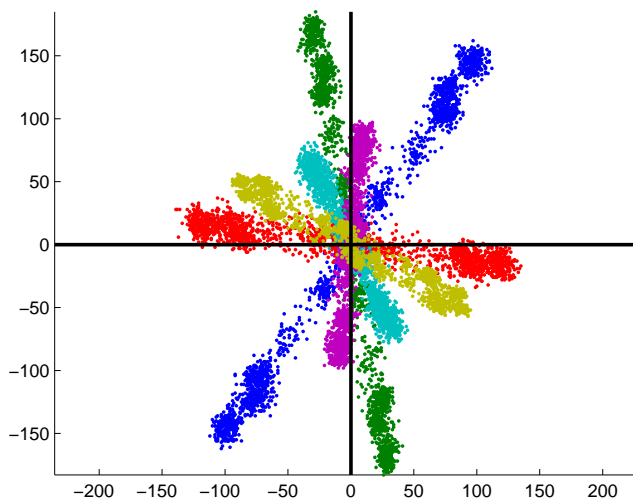


**Figure 4.2:** Typical IQ constellation

## 4.1 Number of signals estimation

AIC and MDL were used to estimate the number of signals impinging on the antenna array. Unfortunately, regardless of the measurement sites, the estimated signal counts were always equal to 4, that is the maximum that can be solved by a 5-element FBSS subarray. This estimation was apparently not correct because as shown in section 4.3, assuming a single incoming signal results in relatively good results. This failure is a critical issue since the MUSIC algorithm requires the knowledge of the signal counts. So in the analysis we can only make assumptions about the number of signals.

The working principle of AIC and MDL algorithms is based on the value gap between the signal and noise eigenvalues. Particularly, the noise eigenvalues are represented by a cluster of the smaller eigenvalues. Table 4.1 shows eigenvalues of the signal covariance matrix from simulations and measurements. For the simulation, there are four cases presented, namely 1, 2, 3, and 4 correlated signals impinging on a six-element ULA. In each case, the received signals are FBSS pre-processed, which result in a 5x5 covariance matrix. It can be seen in the case of 1, 2, and 3 signals that the smaller eigenvalues are almost equal, and form a cluster.

In contrast, eigenvalues of the measurement covariance matrix are monotonically decreasing, and there is no a clear cluster formed. Consequently, the function  $MDL(d)$

or  $AIC(d)$  never rebound as the  $d$  increases. This is similar with the case of the 4-signal simulation. Note that the exponential term of the measurement eigenvalues is not a concern since the  $MDL$  and  $AIC$  are insensitive to the scaling of eigenvalues.

**Table 4.1:** Eigenvalues of the simulation and measurement data

Data source	Eigenvalues				
Simulation - 1 signal	34.04	<b>1.02</b>	<b>0.99</b>	<b>0.98</b>	<b>0.96</b>
Simulation - 2 signals	53.46	7.12	<b>1.03</b>	<b>1.00</b>	<b>0.98</b>
Simulation - 3 signals	52.8	23.6	1.58	<b>1.00</b>	<b>0.99</b>
Simulation - 4 signals	55.5	22.09	16.4	1.50	<b>0.90</b>
Measurement	$3.461 \times 10^4$	$0.425 \times 10^4$	$0.150 \times 10^4$	$0.034 \times 10^4$	$0.015 \times 10^4$

## 4.2 Effect of calibration

To examine the effect of calibration, only four channels, namely channel 3, 4, 5, and 6 are used. The other two channels are not included because they have an obviously different cable length and will certainly result in large errors. Figure 4.3 shows the DOA histograms of the four channels that are computed using the MUSIC algorithm. Both cases show relatively consistent results. It turns out that the degree of phase shift (Table 3.1) in the uncalibrated array does not influence the accuracy by much. And it is more surprising that the uncalibrated array has a lower average RMSE, that is at  $2.12^\circ$ . Whereas the average RMSE of the calibrated one is at  $2.79^\circ$ .

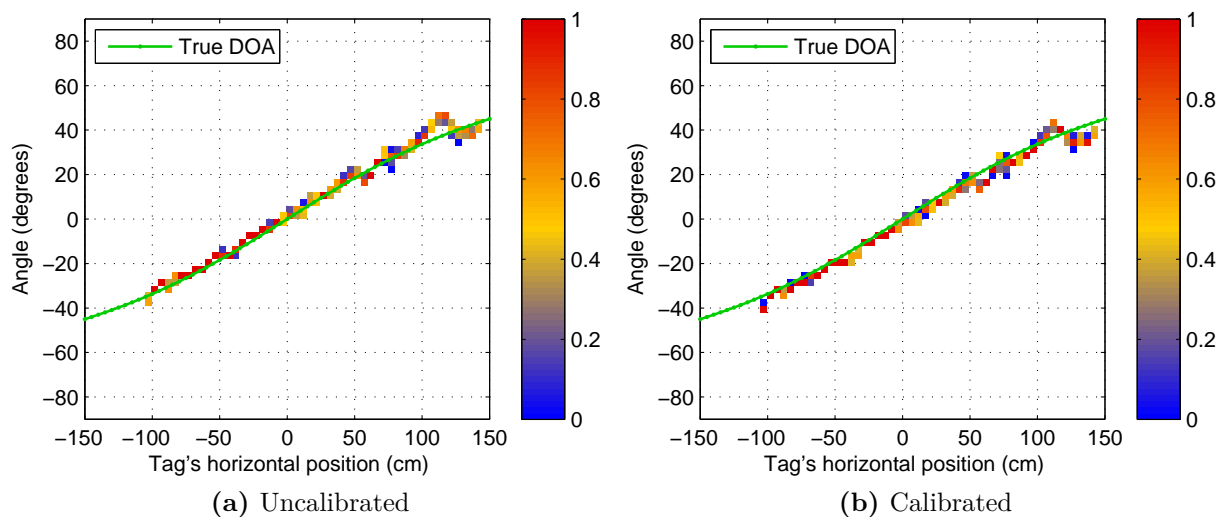


**Figure 4.3:** Histogram per DOAs, MUSIC, tag's height at 150 cm

According to Equation 2.16, the MUSIC power will be higher if the steering vector and the noise eigenvectors are more orthogonal. This orthogonality will occur if the noise and signal subspaces are well separated. A good subspace separation can be obtained when the received signals truly represent the source signals.

A closer look at the MUSIC spectrum of each observation actually confirms the efficacy of calibration. Figure 4.4 serves as an example of the MUSIC spectrum comparison between the calibrated and uncalibrated array. It can be seen that the MUSIC power of the calibrated array is in fact higher than that of the uncalibrated one. This strongly indicates that the calibrated signals more genuinely describe the source signals. The fact that the calibrated array has a lower accuracy is most likely caused by inaccurate placement of the array center point. Shifting the green line in Figure 4.3 is equivalent to moving the array center point. Intuitively, if the green line in Figure 4.3b is shifted a little bit downward, then the estimated DOAs will be closer to the true DOA.

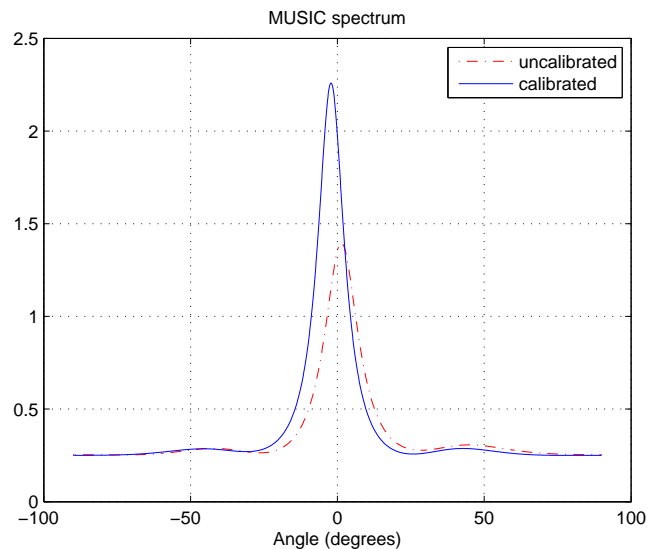


**Figure 4.4:** MUSIC spectrum of the calibrated and uncalibrated array

### 4.3 Measurements in reflection-minimum environments

The SmartXP Lab is a room with an area and height of  $6 \times 7.5 \text{ m}^2$  and 5.5 m. With such dimensions, SmartXP Lab provides an echo-minimum environment because when the unwanted signals reflect back to the phased-array, they would have traveled a long distance and therefore substantially lost their power. Figure 7.1 shows a photograph of the SmartXP Lab. The following sections discuss the measurement results at various tag's heights and the effect of FBSS.

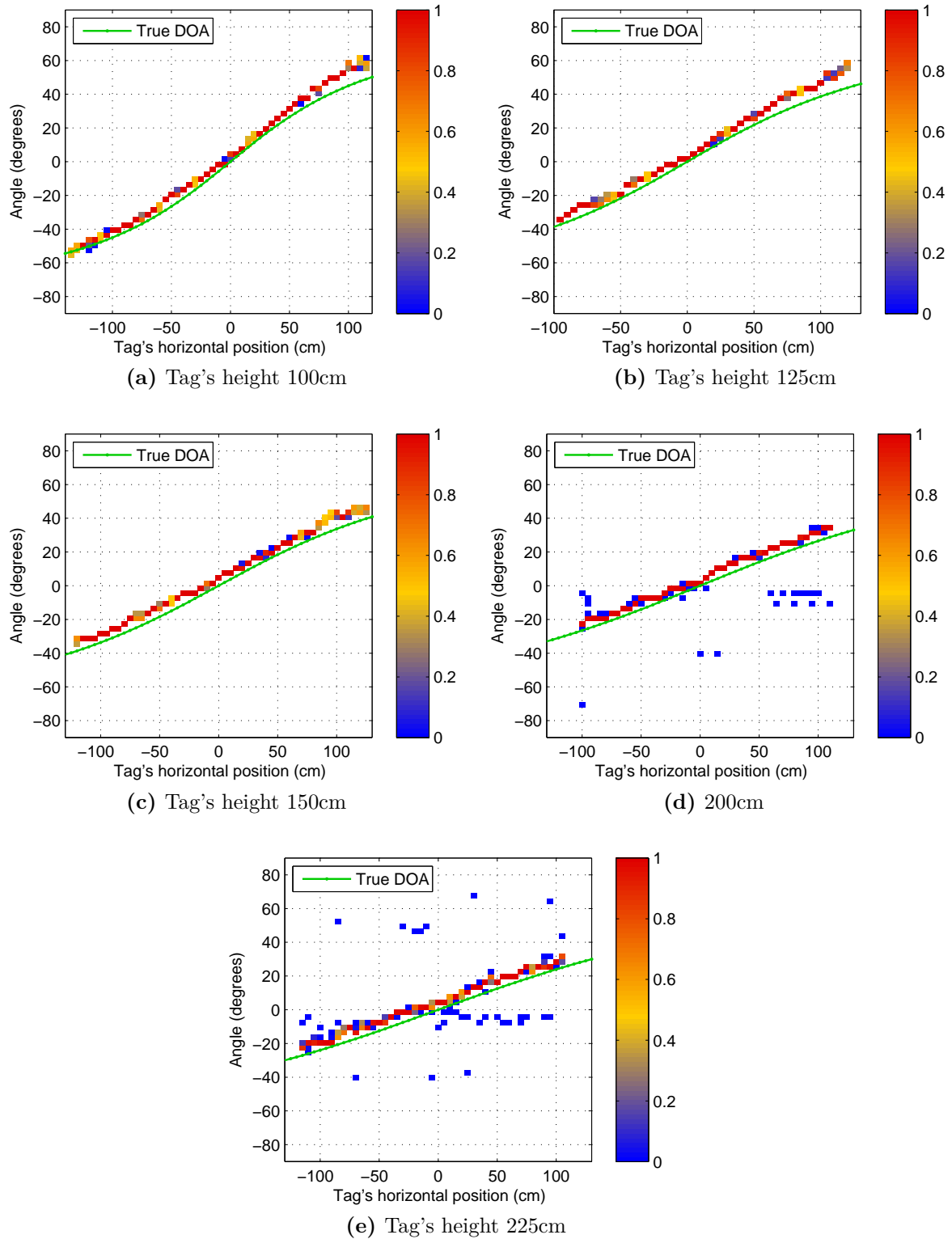


Figure 4.5: SmartXP, MUSIC, non-FBSS, 1 signal assumed – at several heights

## Without FBSS – varying heights

In this section we will examine the system’s performance at several tag’s heights, i.e. 100 cm, 125 cm, 150 cm, 200 cm, and 225 cm. The data are analyzed using the non-FBSS MUSIC algorithm. The MUSIC algorithm requires the knowledge of the signal counts. Both AIC and MDL algorithm estimate 4 signals (with FBSS) or 5 signals (without FBSS) present all the time. However, this is apparently not true as we will see in the next section. Considering the reflection-minimum environment in SmartXP Lab, it is reasonable to use a single signal assumption.

Like shown in Figure 4.5, at the heights of 100 cm, 125 cm, and 150 cm, the estimated DOAs are fairly consistent with the true DOAs although the trending lines are slightly higher than that of the true DOAs. This may be jointly caused by several factors, namely the exclusion of antenna in the calibration section 3.2, not satisfying the far-field assumption, and tag’s height misplacement because of human error.

Unlike the others, measurements at 200 cm and 225 cm exhibit erroneous DOA estimations. Despite the presence of the outliers, the general trends still agree with the true DOA. By investigating the received data, it is immediately clear why there are numerous outliers. It turns out that the outliers have peculiar IQ constellations like shown in Figure 4.6. In fact the measurements at 200 cm and 225 cm were done on a different day than the others. The source of problem was not further investigated. But it was speculated that some wideband stray signals jumped into the frequency of interest. The best solution is to identify and isolate the root of the problem. But if somehow it is not possible, then a pragmatic solution is to asses the shape of the IQ constellations, for example using Pearson product-moment correlation coefficient. Then, these sporadically happening unusual shapes can be discarded.

Table 4.2 shows the average of all positions’ Root Mean Square Error (RMSE) of measurements in SmartXP Lab using the MUSIC algorithm. Based on Figure 4.5 and Table 4.2, it can be concluded that a single signal assumption fits well with the actual measurements.

**Table 4.2:** Average RMSE of measurements in SmartXP Lab

Height (cm)	100	125	150	200	225
Average RMSE (degree)	4.79	4.75	5.27	4.8	5.45

## With FBSS

In this section, we choose one representative tag’s height, i.e. at 150 cm and examine the effect of applying FBSS. With a six-element array, the maximum number of signals that can be solved is four. However, since knowledge of the signal counts is not available, it is constantly assumed that either 1, 2, 3, or 4 signals are present all

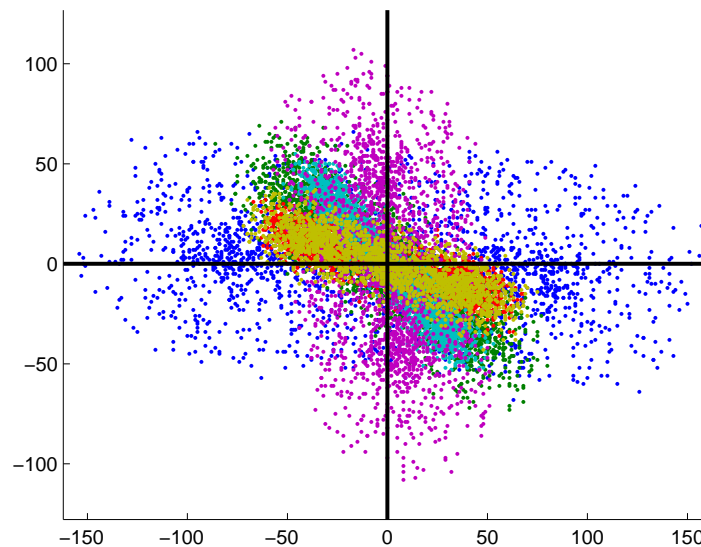


**Figure 4.6:** IQ constellations of the outliers

the time. With the multiple signals assumption, the MUSIC algorithm indeed will produce multiple peaks, and one of the strongest is determined as the true DOA. However the highest peak does not correspond to the strongest signal. Instead, it can be calculated using Equation 2.29.

It is evident in Figure 4.7 that one signal assumption fits best with the true DOA. Nevertheless, in the case of the two signals assumption, the peak with the highest power can still be determined correctly most of the time, with only few outliers. Whereas in the case of three and four signals, the estimations become increasingly worse. Therefore, it can be concluded that only one signal is present in the SmartXP measurements.

## 4.4 Measurements in reflective environments

Under reflection-minimum environments, the system has been found to perform very well. To investigate the performance in a more realistic environment comparable to retail shops, measurements were done in Zilverling office building, University of Twente. There were three environment settings being used, namely *Office-1*, *Office-2*, and *Hallway*.

The Office-1 setting is a room with an area and height of  $3 \times 7.5 \text{ m}^2$  and 3 m, respectively. It contains tables, chairs, and computers. The phased-array was placed in the middle of the room. The surrounding walls and ceiling above are made from non metallic materials. Figure 7.2 shows the situation in Office-1. Office-2 is actually the

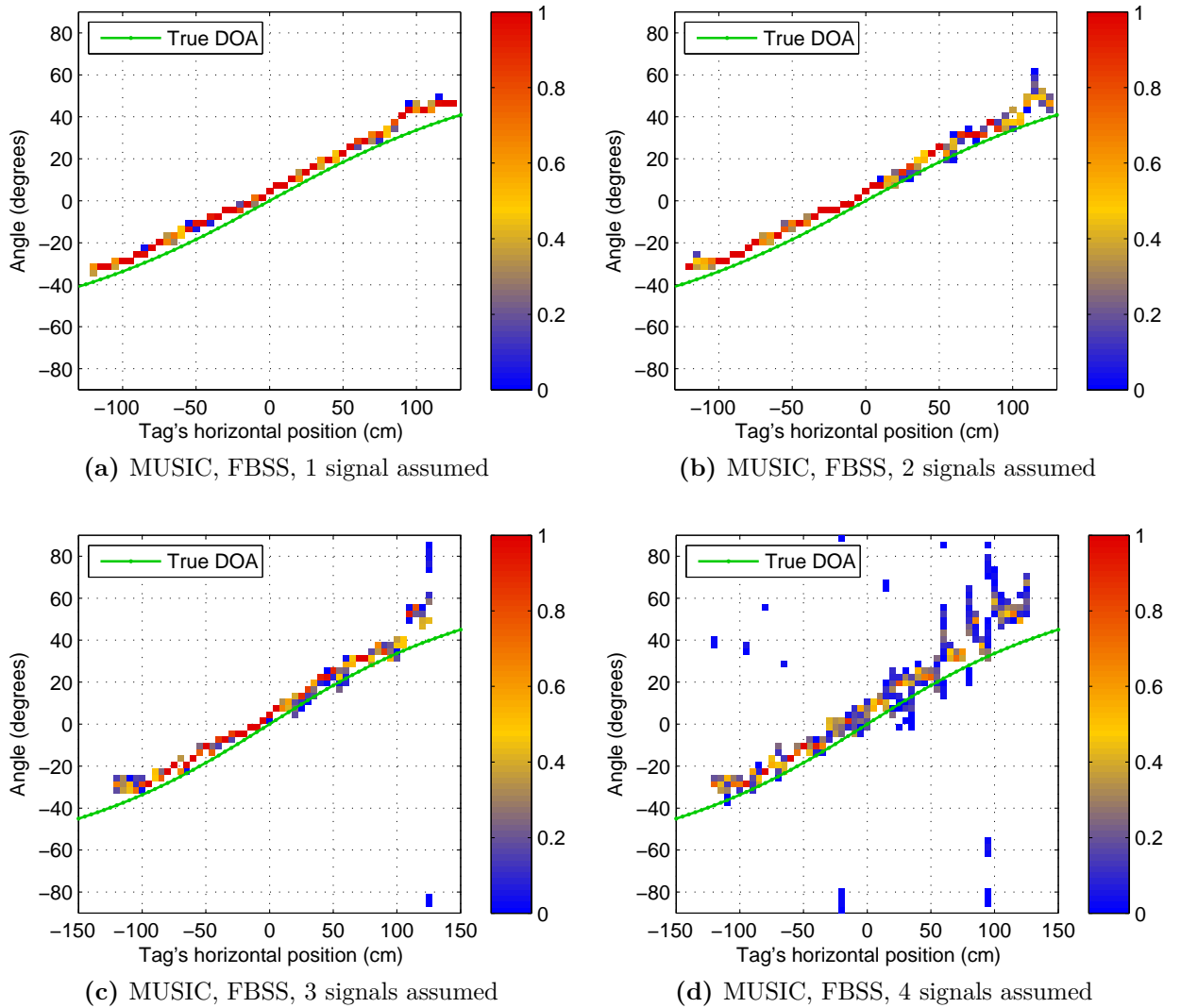


**Figure 4.7:** SmartXP, MUSIC, FBSS, tag's height at 150 cm

same room as Office-1, except that the phased-array was placed on the side of the room, which effectively behaves like a smaller room. Moreover, the ceiling is lower and covered by a metal grid. Figure 7.3 depicts the Office-2 setting. Lastly, in the Hallway setting, the phased-array was positioned at the end of a hallway that has a width and height of xx m and xx m, respectively. More detail about the Hallway setting can be found in Figure 7.4.

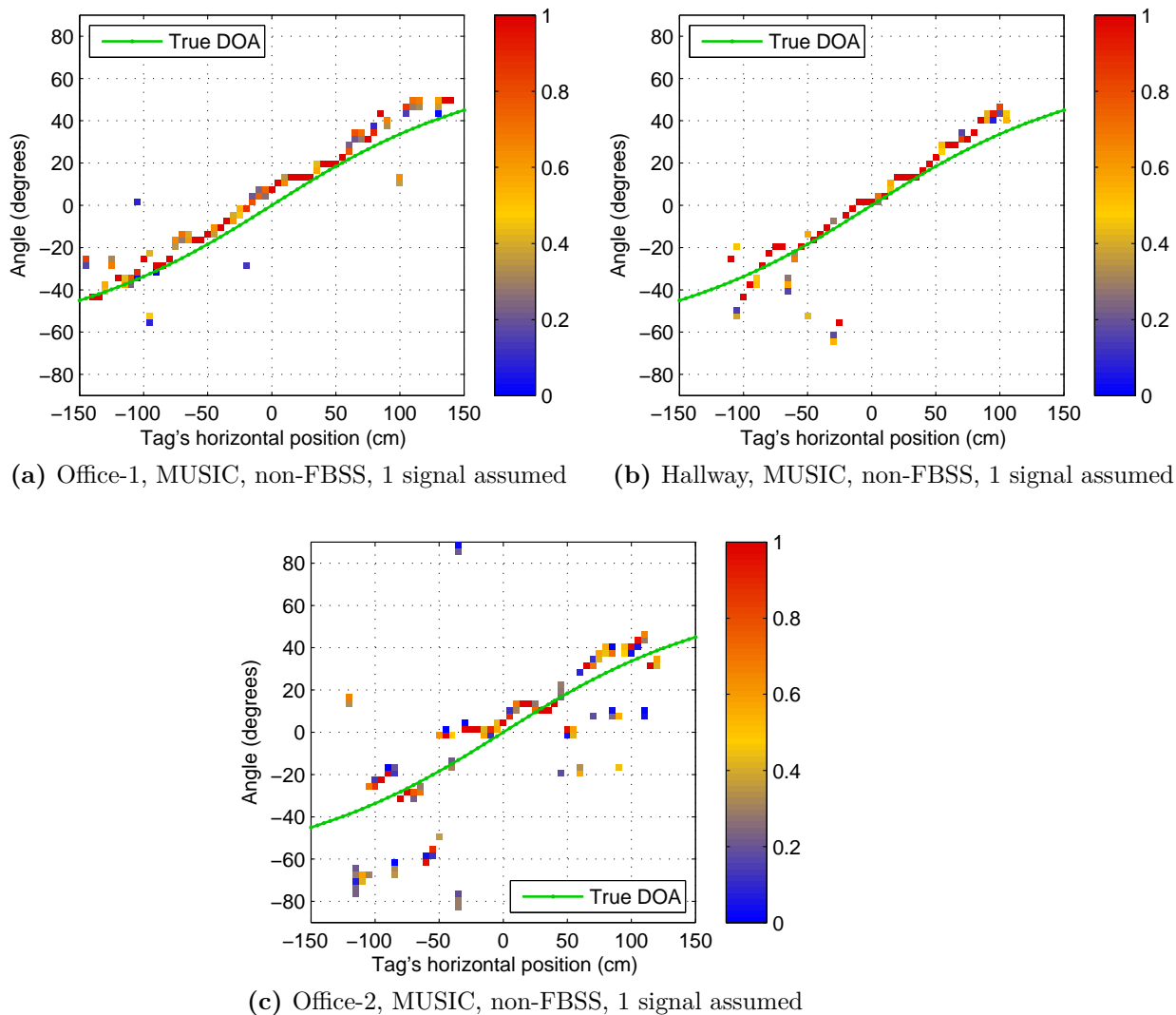


Figure 4.8: Reflective environments, tag's height at 150 cm

## Without FBSS

First, we will apply the plain MUSIC algorithm and hold a single signal assumption. Figure 4.8 shows that in Office-1, Office-2, and Hallway settings the estimated DOAs

have become worse, indicated by the presence of more outliers. The worst results that are evident in the Office-2 is most likely due to the metal grid ceiling that behaves like a strong reflector. Although in Office-1 and Hallway the general trends still agree with the true DOAs, outliers appear at some points. This indicates that the environment is not uniform. Probably there is more multipath at the points where outliers happen.

## With FBSS

Analysis with plain MUSIC has shown that at some points the estimation errors are unacceptably large, which may be caused by the presence of multipath signals. In this section, we will apply FBSS MUSIC algorithm to overcome the multipath.

Again, since the number of impinging signals is not known, it is constantly assumed that there are either 1, 2, 3, or 4 signals all the time. The complete histogram figures can be found in Appendix Figure 7.5, Figure 7.6, and Figure 7.8. It can be seen that unfortunately FBSS MUSIC is not able to improve the DOA estimates.

In fact, observations show that the true DOA occasionally occurs among the multiple peaks in the MUSIC spectra. However the true DOA somehow has a lower power than others, and thus the correct DOA is not selected. Going from this fact, it may be helpful to use beamforming algorithms whose power spectrum is the actual signal strength. Also, the number of signals is not required in beamforming algorithms and we are only interested in the strongest DOA.

Figure 7.7 and Figure 7.9 show the results of using FBSS-classical and FBSS-MVDR beamforming in Hallway and Office-2 settings. It turns out that the classical and MVDR beamforming are not able to improve the DOA estimates either.

**Table 4.3:** Average RMSE of measurements in several sites, tag's height at 150 cm

Analysis \ Site	Office-1	Hallway	Office-2
MUSIC, non-FBSS	6.92	7.61	14.93
MUSIC, FBSS, 1 signal assumed	7.51	8.42	15.74
MUSIC, FBSS, 2 signal assumed	8.2	7.77	15.68
MUSIC, FBSS, 3 signal assumed	9.1	8.31	16.74
MUSIC, FBSS, 4 signal assumed	14.3	11.28	22.51
Classical beamforming	-	8.3	11.49
MVDR	-	10.10	14.37

Table 4.3 summarizes the average RMSE of all settings. The measurement in Office-1 has the lowest RMSE which may be explained by the fact that it has a larger dimension. Whereas Office-2 has the highest RMSE, and this is most likely influenced by the metal grid ceiling.

## 5 Conclusions

A six-element linear phased-array for estimating DOA of UHF RFID tags has been implemented. It was found that the difference in cable lengths and non-uniformity of the electronic components among the channels introduced undesired phase shifts on the IQ data. Such a systematic error was corrected by performing calibration on the channels.

The system's performance was evaluated under both reflective-minimum and reflective environments. Regardless of the environments, the MDL and AIC algorithm were unable to correctly estimate the number of signals received by the phased-array. This failure posed a critical problem since the subspace based algorithms, like MUSIC, require the knowledge of the signal counts. So, in the MUSIC algorithm analysis we could only assume there were either one, two, three, or four signals received by the phased-array.

The measurements done at the tag's height from 100 to 225 cm in the reflective-minimum environment showed relatively consistent results with an average RMSE less than  $5.45^\circ$ . However, the measurements done in the reflective environments exhibited significant deterioration. The smaller the room size and the presence of a large metal grid apparently caused the appearance of more outliers. While showing a promising simulation result in solving multipath signals, it was found that unfortunately FBSS algorithm was *not* able to improve the real measurement in the reflective environments. One possible explanation is that the number of multipath signals is more than the maximum number solvable by the current six-element phased-array. Alternatively, it could be that the multiple signals are closely spaced such that they are not separable anymore.



## 6 Recommendations

Further extending the current six-element receiver, which has a length of 1 meter, may not be practical anymore unless a higher frequency UHF RFID technology like 2.4 GHz is used. On the other hand, the transmitter currently being used only consists of one antenna. It can be extended to use multiple antennas and form a phased-array. By doing so, the transmitter can have a narrower and steerable beam pattern. Such a transmitter array is said to be able to reduce the effect of multipath by pointing the beam direction toward the desired tag and nulling the interferers [Kar10].

In a real deployment, the phased-array is preferably to be installed on a ceiling. So the phased-array will face a floor possibly made of concrete. The system was not tested under such a setting yet. Such a set-up might have very different performance since the reflection characteristics of a concrete floor might differ to a large extent from the characteristics of a ceiling.



## 7 Appendix

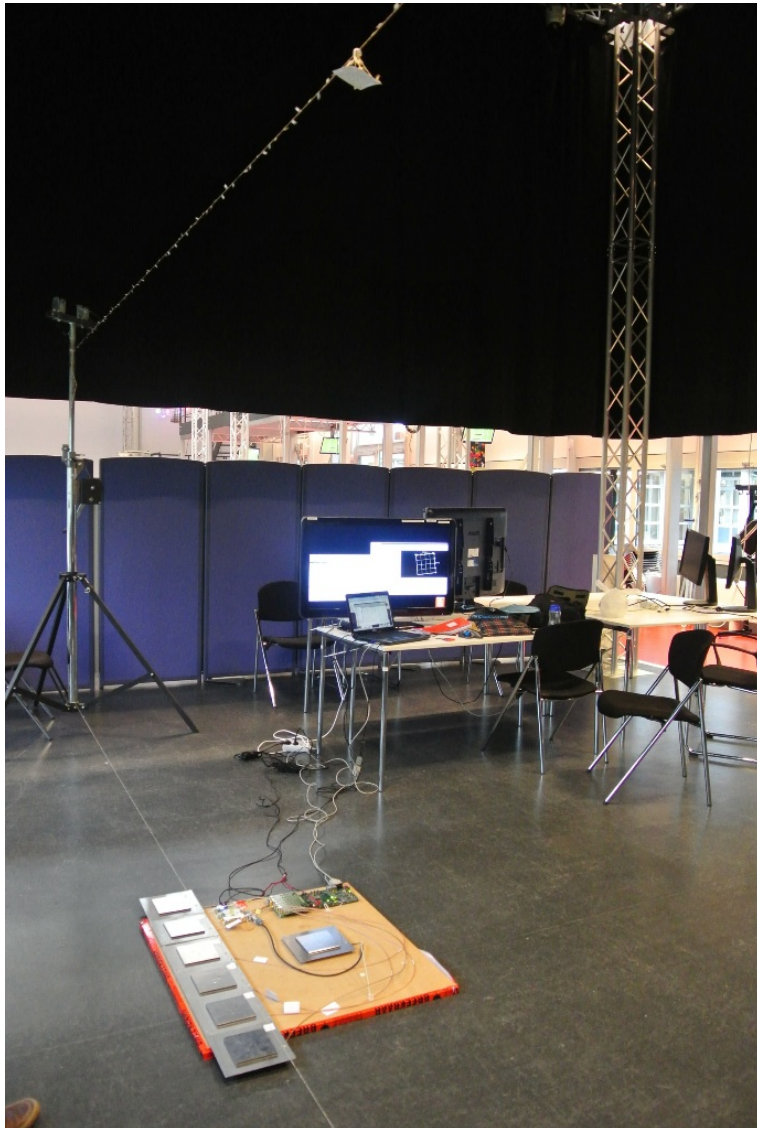


**Figure 7.1:** SmartXP Lab

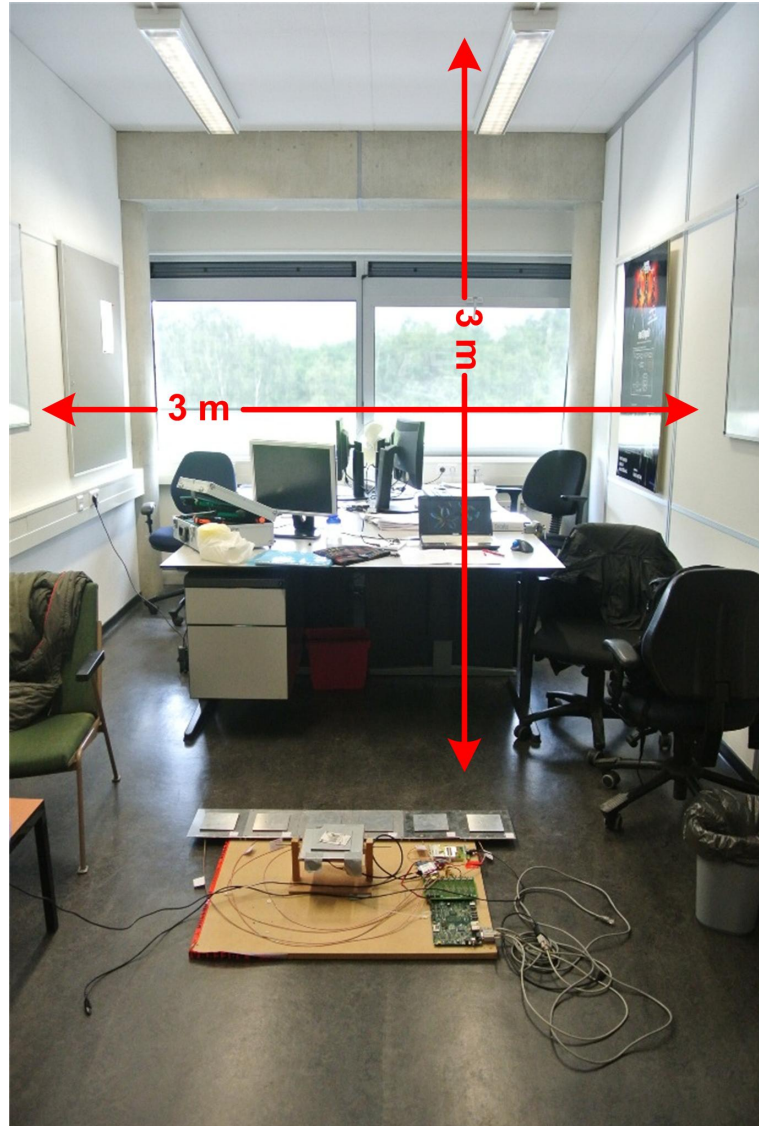
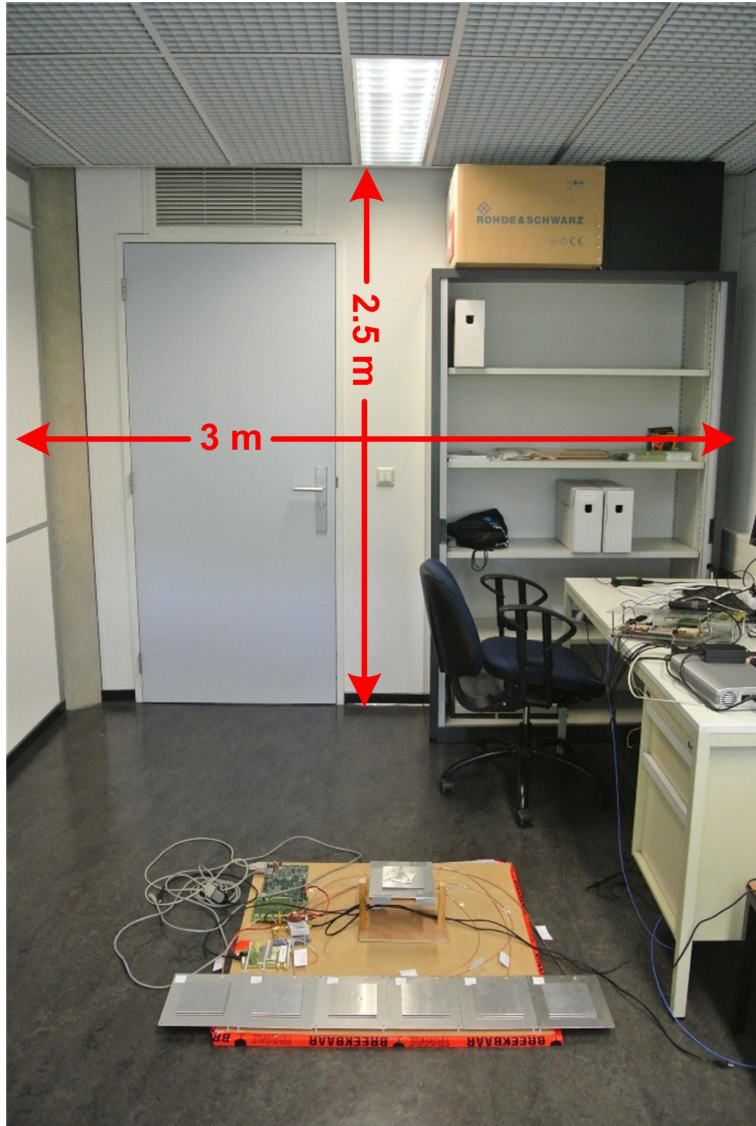


Figure 7.2: Office-1



**Figure 7.3:** Office-2, with metal grid ceiling

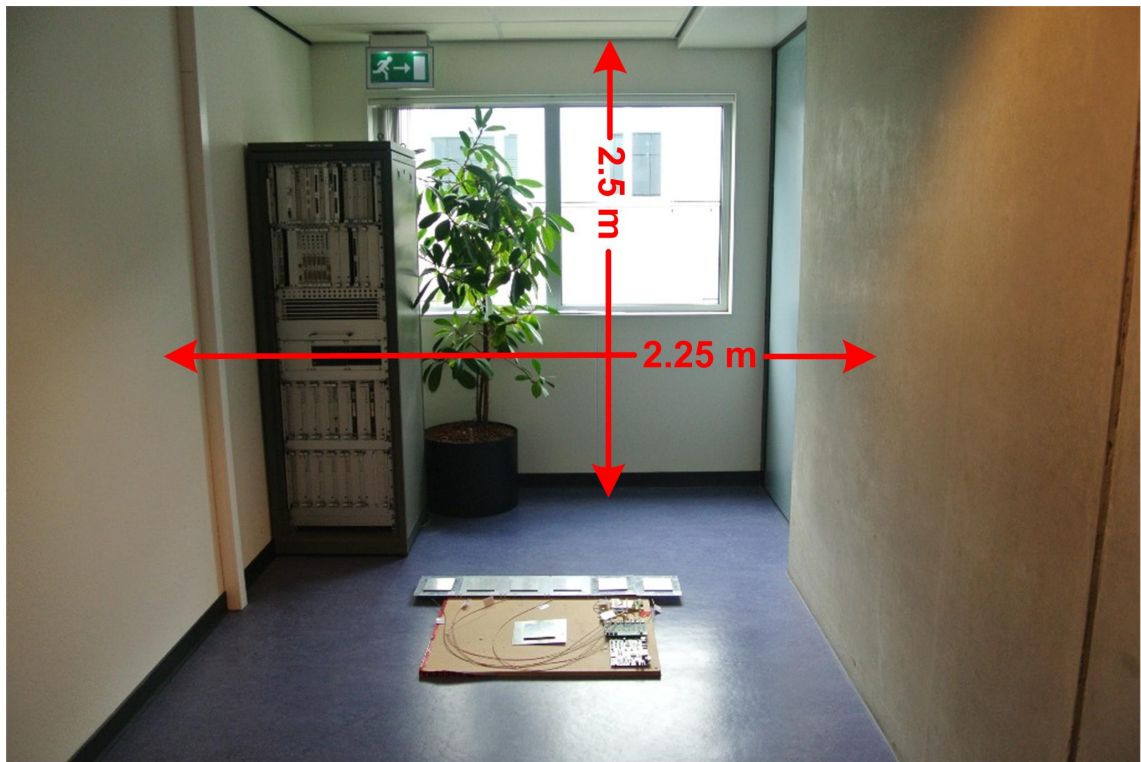


Figure 7.4: Hallway

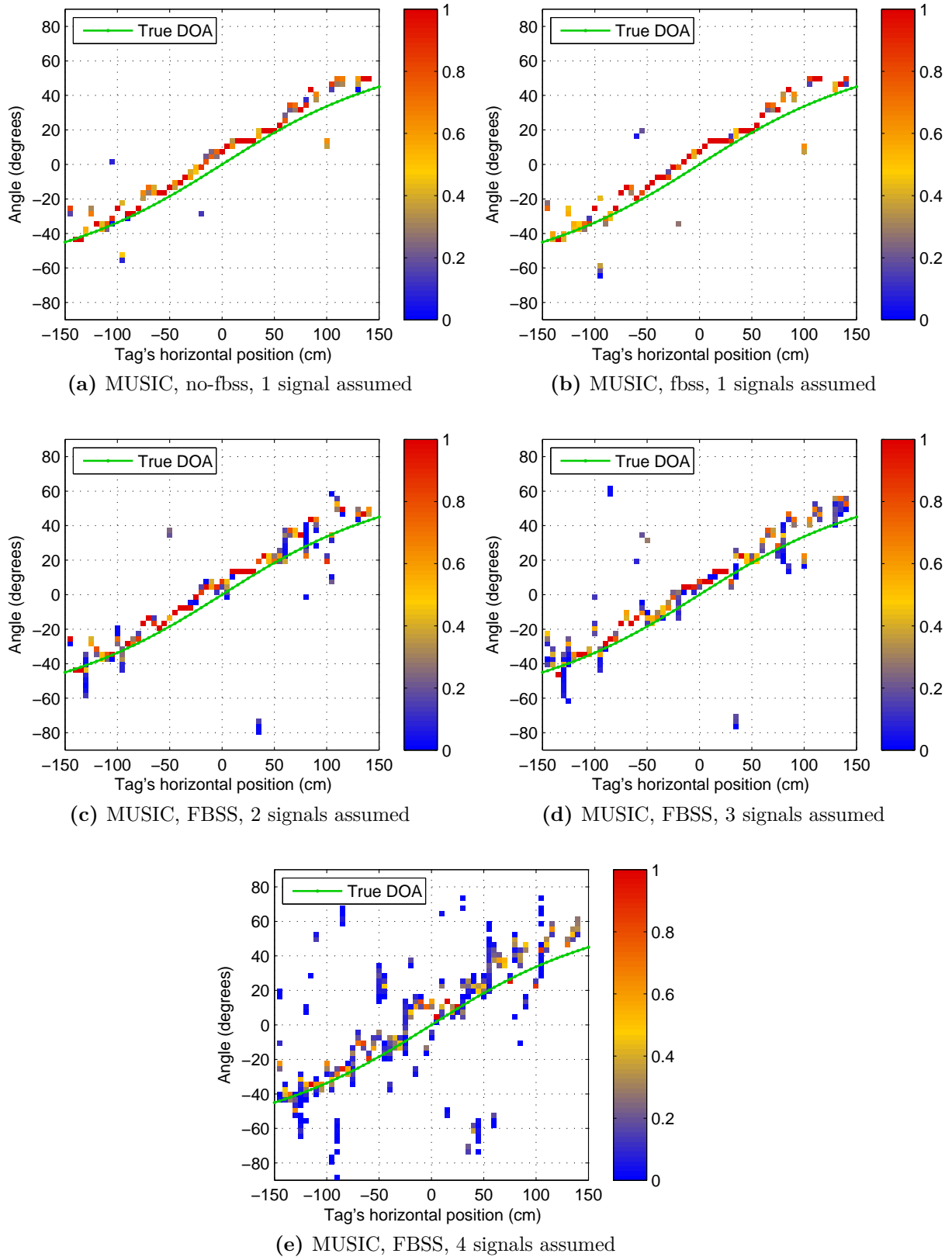
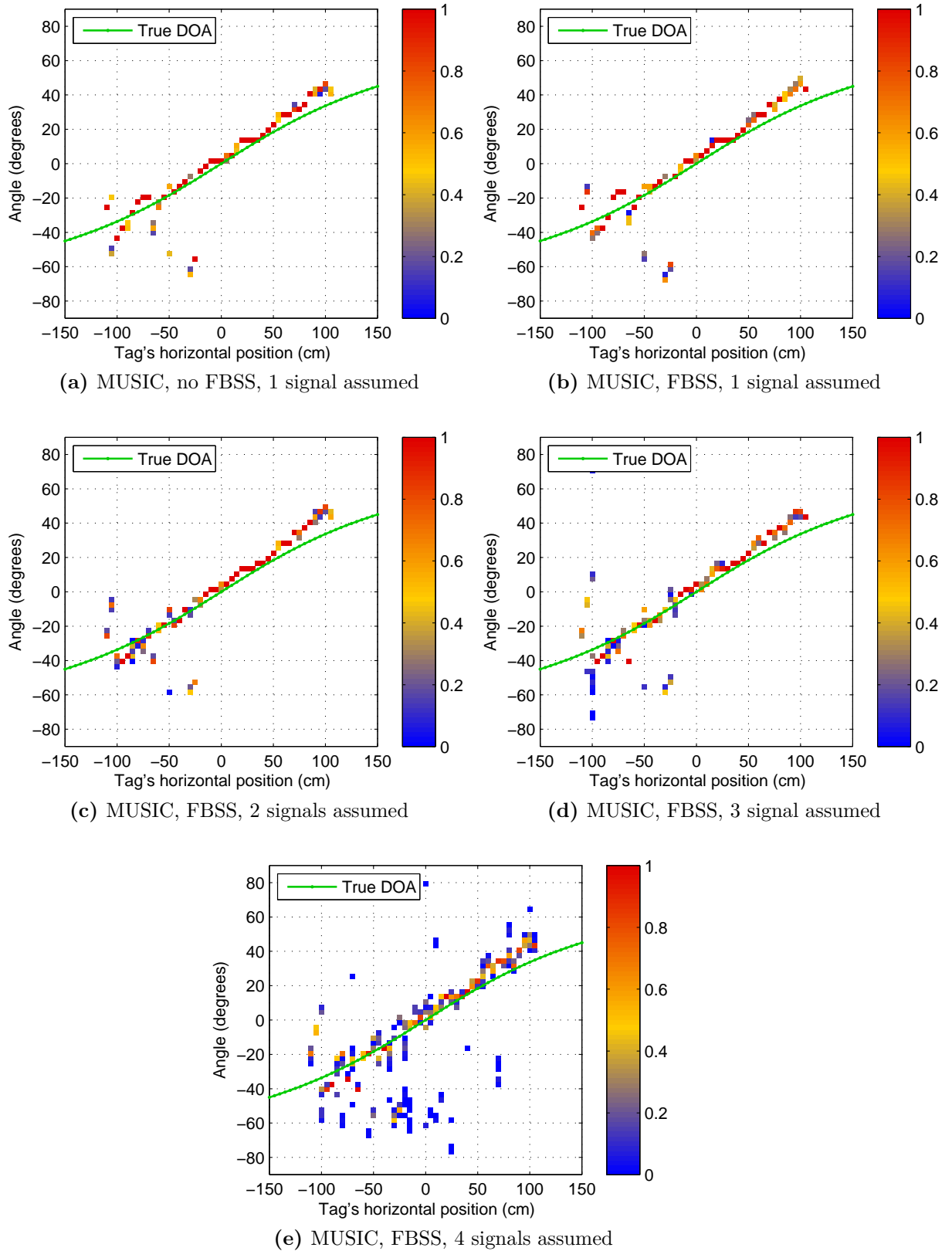
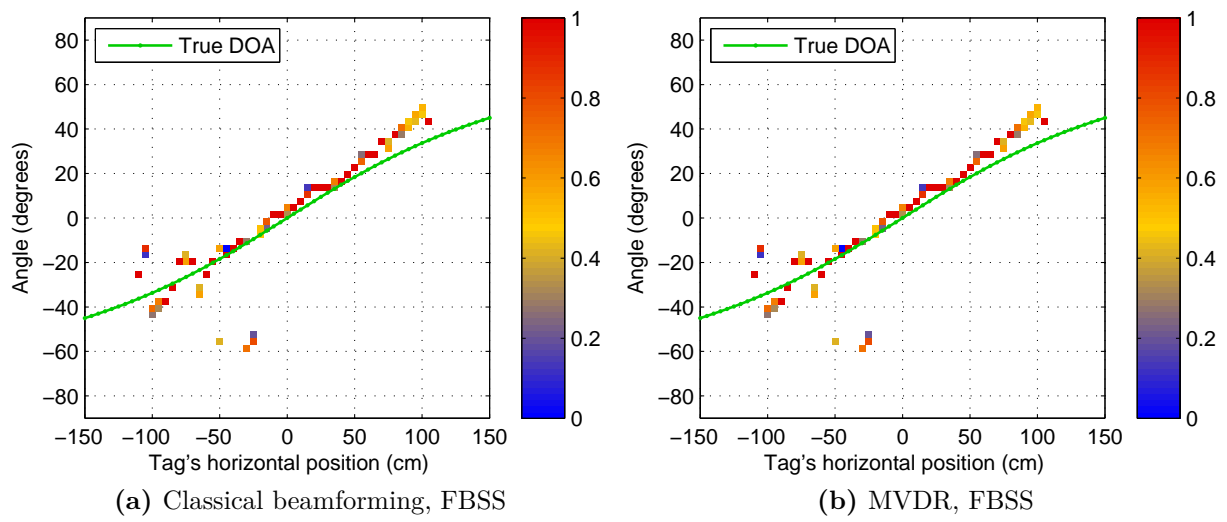


Figure 7.5: Histograms of Office-1, 150 cm high



**Figure 7.6:** Histograms of Hallway, 150 cm high, MUSIC



**Figure 7.7:** Histograms of Hallway, 150 cm high, beamforming

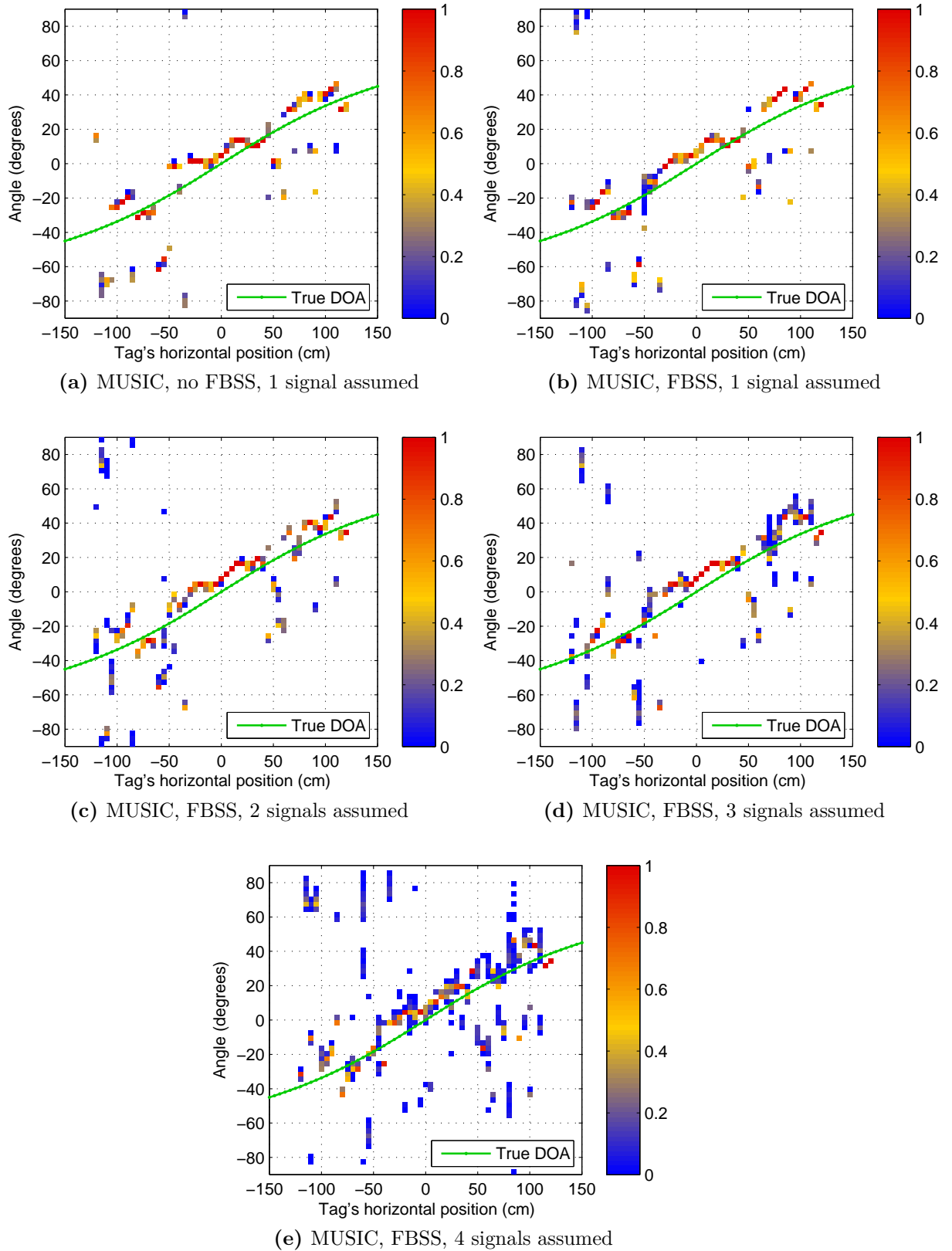


**Figure 7.8:** Histograms of Office-2, 150 cm high, MUSIC

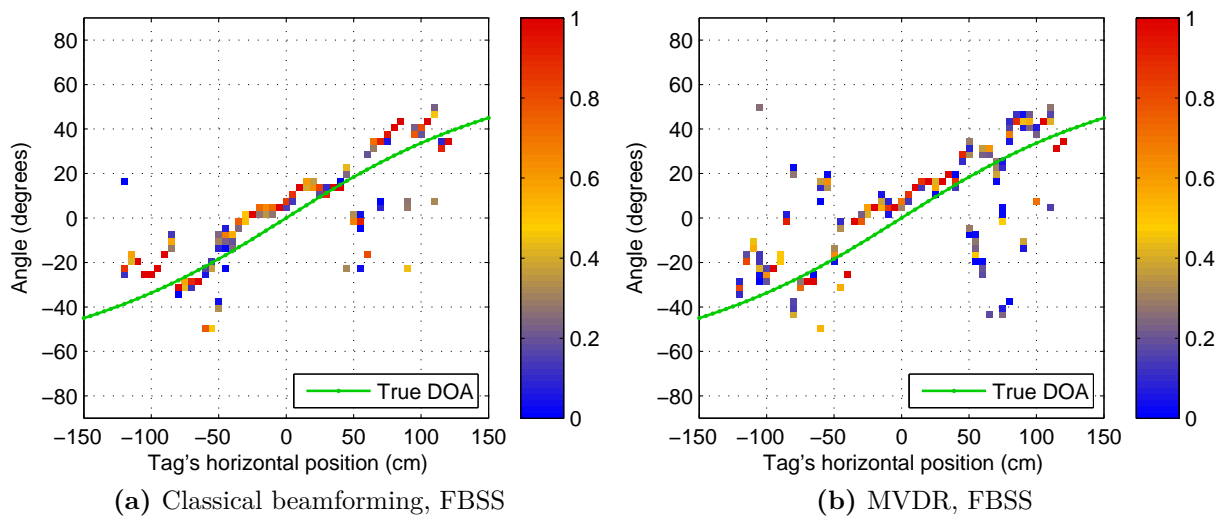


**Figure 7.9:** Histograms of Office-2, 150 cm high, beamforming



# Bibliography

- [Ban] Rajeev Bansal. The far-field: How far is far enough? Applied Microwave & Wireless.
- [BBR13] Alexey Borisenko, Miodrag Bolic, and Majed Rostamian. Intercepting uhf rfid signals through synchronous detection. *EURASIP J. Wireless Comm. and Networking*, 2013:214, 2013.
- [Dob08] Daniel M. Dobkin. *The RF in RFID*. Newnes, 2008.
- [DS13] R. B. Darling and W. Sun. Transmission lines and reflected signals. <http://www.ee.washington.edu/faculty/darling/AgilentRFLab/labs.html>, September 2013.
- [epc14] [http://www.gs1.org/epcglobal/implementation#case\\_studies](http://www.gs1.org/epcglobal/implementation#case_studies), January 2014. 26.
- [Fin10] Klaus Finkenzeller. *RFID Handbook*. John Wiley & Sons, 2010.
- [Ins13] National Instruments. Advanced rfid measurements: Basic theory to protocol conformance test. <http://www.ni.com/white-paper/6645/en/>, December 2013.
- [Kar10] N. C. Karmakar. *Recent Paradigm Shift in RFID and Smart Antennas, in Handbook of Smart Antennas for RFID Systems (ed N. C. Karmakar)*. John Wiley & Sons, Inc, 2010.
- [KV96] H. Krim and M. Viberg. Two decades of array signal processing research: the parametric approach. *Signal Processing Magazine, IEEE*, 13(4):67–94, 1996.
- [Mat] Wolfram MathWorld. Rotation matrix. <http://mathworld.wolfram.com/RotationMatrix.html>.
- [Mol10] Andreas F. Molisch. *Wireless Communications*. Wiley - IEEE, 2010.
- [PK89] S.U. Pillai and B.H. Kwon. Forward/backward spatial smoothing techniques for coherent signal identification. *Acoustics, Speech and Signal Processing, IEEE Transactions on*, 37(1):8–15, 1989.
- [SB08] Jeffrey Foutz; Andreas Spanias; and Mahesh K. Banavar. *Narrowband Direction of Arrival Estimation for Antenna Arrays*. Morgan & Claypool, 2008.

- [Sch86] R.O. Schmidt. Multiple emitter location and signal parameter estimation. *Antennas and Propagation, IEEE Transactions on*, 34(3):276–280, 1986.
- [SWK85] Tie-Jun Shan, M. Wax, and T. Kailath. On spatial smoothing for direction-of-arrival estimation of coherent signals. *Acoustics, Speech and Signal Processing, IEEE Transactions on*, 33(4):806–811, 1985.
- [Tre02] Harry Van Trees. *Optimum Array Processing*. John Wiley & Sons, 2002.
- [vL13] R.G.J.F.O.J. van Lakwijk. Tracking of uhf rfid tagged stock in retail. Master’s thesis, University of Twente, 2013.
- [XZS07] Jingmin Xin, Nanning Zheng, and A. Sano. Simple and efficient non-parametric method for estimating the number of signals without eigendecomposition. *Signal Processing, IEEE Transactions on*, 55(4):1405–1420, 2007.
- [ZCY10] Gopal K. Gokeda Zhizhang Chen and Yiqiang Yu. *Introduction to Direction-of-Arrival Estimation*. Artech House, 2010.